

# Global Organization of Three-Dimensional, Volume-Preserving Flows: Constraints, Degenerate Points, and Lagrangian Structure

Bharath Ravu,<sup>1, a)</sup> Guy Metcalfe,<sup>2, b)</sup> Murray Rudman,<sup>3, c)</sup> Daniel R. Lester,<sup>4, d)</sup> and Devang V. Khakhar<sup>5, e)</sup>

<sup>1)</sup>*IITB-Monash Research Academy, Indian Institute of Technology Bombay, Powai, Mumbai-400076, India.*

<sup>2)</sup>*School of Engineering, Swinburne University of Technology, Hawthorn, VIC 3122, Australia*

<sup>3)</sup>*Department of Mechanical and Aerospace Engineering, Monash University, Clayton, VIC 3800, Australia*

<sup>4)</sup>*School of Engineering, RMIT University, Melbourne, VIC 3000, Australia*

<sup>5)</sup>*Department of Chemical Engineering, Indian Institute of Technology Bombay, Powai, Mumbai-400076, India*

(Dated: 13 November 2019)

Global organization of 3-dimensional (3D) Lagrangian chaotic transport is difficult to infer without extensive computation. For 3D time-periodic flows with one invariant we show how constraints on deformation that arise from volume-preservation and periodic lines result in resonant degenerate points that periodically have zero net deformation. These points organize all Lagrangian transport in such flows through coordination of lower-order and higher-order periodic lines and prefigure unique transport structures that arise after perturbation and breaking of the invariant. Degenerate points of periodic lines and the extended 3D structures associated with them are easily identified through the trace of the deformation tensor calculated along periodic lines. These results reveal the importance of degenerate points in understanding transport in one-invariant fluid flows.

**Global organization of 3-dimensional (3D) Lagrangian chaotic transport is difficult to infer without extensive computation. For 3D time-periodic flows with one invariant we show how constraints on deformation from volume-preservation and periodic lines cause resonant degenerate points that periodically have zero net deformation. These points organize all Lagrangian transport in the flow through coordination of lower-order and higher-order periodic lines. We also show how to easily identify degenerate points of periodic lines and the extended 3D structures that go with them.**

## I. INTRODUCTION

Design and control of Lagrangian fluid particle trajectories in three-dimensional (3D) incompressible flow fields (conservative dynamical systems) is a key step toward engineering efficient mixing and transport properties for fluid devices. This is particularly important for intrinsically low Reynolds number applications, such as microfluidic devices, processing highly viscous or delicate materials, and many others<sup>1</sup>. Due to considerations of simplicity or ease of manufacture, devices often have spatial symmetries and time periodicity. In the presence of

such symmetries, the dynamical system of the 3D incompressible flow has invariants or conserved quantities<sup>2,3</sup>. What organizes the global Lagrangian transport structure in such a flow? The answer is not completely known<sup>4</sup>, but fluid deformation around periodic lines plays an important role. Here we show how in the Stokes limit constraints imposed by volume-preservation and by a lack of deformation in the tangent direction to periodic lines organize global 3D transport.

We consider a 3D incompressible time-periodic flow with one invariant that consists of nested topological spheroids, where the effective radial coordinate (or action coordinate) is conserved. Nested spheroids, which we will call shells, conform to Bajer's general formulation of a 3D flow that is nearly everywhere Hamiltonian except in the neighbourhood of stagnation points, where the true 3D character of the flow manifests<sup>5</sup>. Only two-dimensional (2D) flows can be truly Hamiltonian, i.e. have the Lagrangian motion derivable from a stream—or Hamiltonian—function as

$$\frac{dx}{dt} = -\frac{\partial H}{\partial y}, \quad \frac{dy}{dt} = \frac{\partial H}{\partial x}, \quad (1)$$

where  $(x, y)$  are 2D Cartesian coordinates. However in 3D flows with one invariant, motion is restricted to surfaces on which the conserved coordinate is a constant, so that we expect 2D Hamiltonian motion on each shell<sup>1</sup>.

In addition to space-filling shells, the fluid space is shot through with periodic lines (stagnation lines of the flow map) that must either have both ends attached to solid boundaries, or that form closed loops (see appendix B), or that have one or both ends extend to infinity (in an open flow). Periodic lines are a 3D analogue of periodic points in 2D periodic flows: after  $n$  periods, a period- $n$  line is a connected collection of points that all return to their original locations. Typically the lower-order period

<sup>a)</sup>Electronic mail: btrreddy@iitb.ac.in

<sup>b)</sup>Electronic mail: gmetcalfe@swin.edu.au

<sup>c)</sup>Electronic mail: murray.rudman@monash.edu

<sup>d)</sup>Electronic mail: daniel.lester@rmit.edu.au

<sup>e)</sup>Electronic mail: khakhar@iitb.ac.in

lines, e.g. period-1 line (P1 line), are most important for understanding the organization of transport. The closed flow we examine here has the particularly simple situation of having a single P1 line for all parameter values of the flow. Moreover, due to the nature of the flow forcing, the single P1 line is confined to a symmetry plane, making finding the line and analyzing its properties straightforward.

Analogous to 2D periodic points, 3D periodic lines have a locally elliptic or hyperbolic character in that fluid trajectories in the neighbourhood of elliptic line segments rotate around the periodic line, whereas those in the neighbourhood of hyperbolic line segments have a direction of maximal contraction towards the line and a direction of maximal stretching away from the line. Elliptic and hyperbolic segments of a periodic line are separated by degenerate points, where the local deformation is shear-like.

This 2D local motion in the neighbourhood of 3D periodic lines comes about because there is no deformation in the tangent direction of the line. If there were tangent deformation, points of the periodic line would not periodically return to their initial locations. As the spheroidal shells are space-filling, continuity ensures that where a periodic line touches a shell, the line shares its character—elliptic, hyperbolic, or degenerate—with the local Hamiltonian motion on the shell<sup>6</sup>. For example, where an elliptic segment (e.g. see figure 8) pierces a shell, a Poincaré section on that shell shows an elliptic island centered at the piercing.

No deformation along periodic lines and volume conservation turn out to be stringent—and key—constraints to organization of the flow. In 3D the eigenvalues describing local deformation can be written in terms of the three matrix invariants of the deformation tensor. With two constraints there is only one independent parameter that determines the character of any periodic line. Using these constraints we derive the main results of this paper:

1. Degenerate points of periodic lines are analogous to resonances of classical planar bifurcation theory.
2. Resonances form extended 3D structures coordinating sets of lower-order and higher-order periodic lines.
3. While some of the 3D structures we observe could have been inferred from center manifold theory by expansion in tangent planes about critical points at shell piercings, other observed structures could not have been so inferred. The latter are truly global in nature.
4. There are a finite number of important resonances and associated 3D structures.
5. Because of (1) and (4) one-invariant 3D flows can be completely understood hierarchically by easily finding the resonant degenerate points and their extended transport structures first on P1 lines, then

on P2 lines, etc., until as much detail of the total Lagrangian transport picture is uncovered as is required for any particular purpose.

Degenerate resonance points and associated structures are generic features of 3D one-invariant flows that previously have been only partially described. While these structures are interesting in themselves, in a sequel publication we will show how this knowledge forms a basis for investigating and understanding how breaking the final invariant in these flows leads to fully 3D transport.

## II. PERIODICALLY REORIENTED ENCLOSED FLOW

In this study we consider a periodically reoriented lid-driven cavity flow as an example of a volume preserving, time-periodic 3D flow with one invariant. Lid-driven cavity flows are one of the most frequently studied problems in computational fluid dynamics<sup>7</sup>; although, there are fewer studies of 3D cavities. The cavity we use is a hemisphere, and we are aware of no previous study of lid-driven flow in this geometry. Importantly, this flow possesses multiple symmetries that makes its Lagrangian properties easy to identify, compute, and study; it is also amenable to experiment.

Lid-driven cavity flow without reorientation admits two families of invariant surfaces (of which manifest as topological cylinders oriented perpendicular to the direction of lid motion) that intersect to form the closed particle trajectories shown in figure 1. The 2D material surfaces associated with these invariants play a strong role in organizing the 3D Lagrangian transport structure into the 1D closed orbits shown in figure 1. What does the periodic reorientation do? Consider the polar decomposition<sup>8</sup> applied to the flow deformation tensor  $\mathbf{F} = \mathbf{R}\mathbf{\Phi}$ , where  $\mathbf{R}$  is a rotation and  $\mathbf{\Phi}$  is a stretching tensor. Instead of describing the deformation at a material point, we can, through an abuse of notation, imagine the decomposition as a prescription of how to generate deformation throughout a material by imposing a sequence of flows followed by rotations. In general, each time interval  $t_n$  could have a different flow map and rotation<sup>9</sup>, leading to a total flow map  $\mathbf{\Psi} = \prod_n \mathbf{R}_n \mathbf{\Phi}_n$ ; however, the more common practice, which we follow here, is to fix  $\mathbf{R}$  and  $\mathbf{\Phi}$ , leading to  $\mathbf{\Psi} = (\mathbf{R}\mathbf{\Phi})^n$  being a function of the time that the flow  $\mathbf{\Phi}$  operates between reorientations and the angle of the rotation. In 2D there is only one reorientation angle, and periodic reorientation has been used to successfully design industrial mixing devices<sup>10</sup>, biomedical diagnostic devices<sup>11</sup>, and subsurface contaminant remediation processes<sup>12,13</sup>. In 3D there could be in general two angles of reorientation. However, in the driven-lid hemisphere only one axis of rotation makes sense, the rotation about the hemisphere radius perpendicular to the lid, and the driven-lid hemisphere is an example of the simplest extension from 2D to 3D of a periodically reoriented flow: a geometry with a 3D flow but only one reorientation angle.

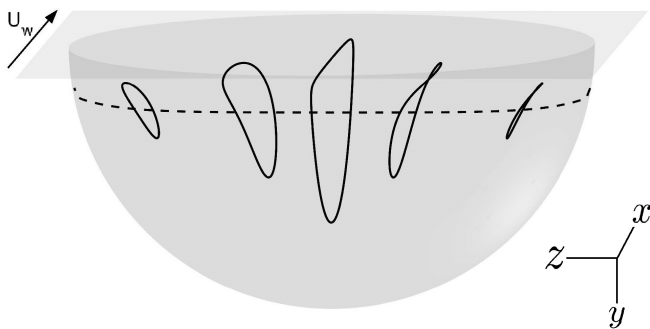


FIG. 1: Schematic of the base flow of the periodically reoriented lid driven hemisphere flow. The lid moves in the  $x$  direction with speed  $U_w$ . Selected streamlines of the base flow are continuous; the stagnation line is dashed.

In the rest of this section we introduce the base flow, discuss the map that corresponds to its periodic reorientation, identify symmetries in the reoriented flow, demonstrate its Hamiltonian nature and briefly introduce the computational methods used to investigate it; full computational details are given in Appendix A.

## A. Periodically Reoriented Hemisphere Flow

### 1. Lid-Driven Hemispherical Cavity Flow

The Periodically Reoriented Hemisphere Flow (PRHF) studied here is a Stokes flow generated in a hemispherical cavity in which the  $x - z$  equatorial plane is driven across the cavity (Figure 1). Distance is normalised by the hemisphere radius,  $R$ , giving a scaled radius of 1. The flow domain is thus defined in spherical polar coordinates by  $r \in [0, 1]$ ,  $\theta \in [0, \pi]$  and  $\phi \in [0, \pi]$  where  $\theta$  is the polar angle and  $\phi$  is the azimuthal angle. We define the base flow as the flow generated with uniform lid motion in the  $\hat{x}$  direction ( $\phi = 0$ ) with steady speed  $U_w$ . The lid velocity is normalised by  $U_w$ , giving a scaled lid velocity of 1.

The base flow consists of one roll with maximum speed at the sliding lid and a stagnation line through the roll centre that is attached to the hemisphere wall (the dashed line in Figure 1) at coordinates  $(0, 0.1624, 0.9867)$  and  $(0, 0.1624, 0.9867)$ . The base flow is constant in time and in the Stokes limit has two symmetries—a fore-aft symmetry (reversal-reflection across the  $z - y$  plane) and a left-right symmetry (reflection across the  $x - y$  plane). With two symmetries all fluid trajectories are closed 1D streamlines (Figure 1).

The equations of motion for the fluid inside the domain are the steady Stokes equation, which gives the momentum balance between viscous and pressure forces as

$$\mu \nabla^2 \mathbf{U} = -\nabla p, \quad (2)$$

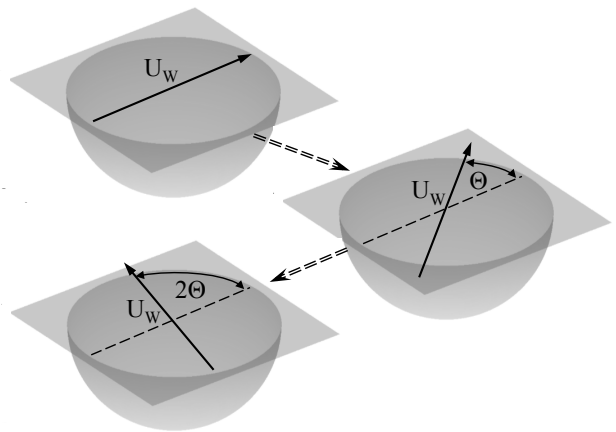


FIG. 2: Schematic showing two steps of reorientation of the base flow by angle  $\Theta$ .

and the conservation of mass or incompressibility condition is

$$\nabla \cdot \mathbf{U} = 0, \quad (3)$$

where  $\mathbf{U}$  is the velocity field,  $p$  is the pressure and  $\mu$  is the viscosity. Although the domain is hemispherical, we calculate the velocity field in cylindrical polar coordinates  $(\rho, \vartheta, z)$  using the spectral-element Fourier code *semtex*<sup>14</sup>. The velocity field is then interpolated spectrally onto a uniform grid in spherical polar coordinates  $(r, \theta, \phi)$  with  $n_r = 100$ ,  $n_\theta = 100$  and  $n_\phi = 320$ . The interpolated cylindrical polar velocity field on this grid is then transformed to spherical polar velocity components  $(v_r, v_\theta, v_\phi)$ . A continuous analytically divergence-free velocity field is created from this grid velocity data using the method of Ravu *et al.*<sup>15</sup>. Finally, MATLAB's ode45 (with relative error  $5 \times 10^{-14}$  and absolute error  $10^{-15}$ ) is used to integrate fluid particle trajectories using the divergence-free velocity field defined analytically at all points inside the hemisphere, and observed Lagrangian coherent structures have been tested to be robust with respect to numerical integration error. The velocity discontinuity at the rim of the sliding lid and hemisphere wall requires special consideration for the numerics; this and additional computational details are in Appendix A.

### 2. Periodic Reorientation

A time-dependant flow is created from the base flow by periodically changing the direction of lid motion, n.b. not through rotation of the lid. The reorientation angle is defined as the angle  $\Theta$  between the directions of successive lid motions, and is one of the key control parameters of the system. The angle of lid motion increases monotonically at each reorientation, with Figure 2 showing the first two such reorientations. In the periodically reoriented flow, the time between reorientations is denoted

by  $\tau$ . Time is non-dimensionalized by  $R/U_w$  giving a non-dimensional period of  $\beta = U_w\tau/R$ . The parameter  $\beta$  is the second key control parameter of the reoriented system.

In the reoriented system, the velocity field satisfies

$$\mathbf{v}(\mathbf{x}, t + \beta) = R_\Theta(\mathbf{v}(\mathbf{x}, t)), \quad (4)$$

or

$$\mathbf{v}(\mathbf{x}, t) = R_{(m\Theta)}(\mathbf{u}(\mathbf{x})), \quad m = \lfloor \frac{t}{\beta} \rfloor \quad (5)$$

for all  $t > 0$ , with  $\lfloor \cdot \rfloor$  the floor function,  $\mathbf{u}$  the base flow velocity field and  $R_\Theta$  the rotation operator for an anti-clockwise rotation about the  $\hat{y}$  axis.

An equivalent—and computationally more convenient—way of defining the time-periodic flow is to move the lid in the  $x$ -direction for a period  $\beta$  followed by rotating the entire flow domain by an angle  $-\Theta$ . In other words, we work with a frame that is invariant with respect to the lid direction. In this way the time periodic flow map is written

$$\Psi_{(\beta, \Theta)} = R_{-\Theta} \Phi_\beta, \quad (6)$$

where  $\Phi_\beta$  is the base flow map for lid displacement  $\beta$  and  $R_{-\Theta}$  is rotation of the hemisphere in a clockwise direction. All analysis will be undertaken with this as the basic building block of the time-periodic flow. We often drop the subscript  $(\beta, \Theta)$  from equation 6 and simply write the time-periodic map as  $\Psi$ , however  $(\beta, \Theta)$  will always be implied. To reduce the complexity of higher dimensions, we always work with trajectories that are stroboscopic with respect to the reorientation period  $\beta$ . In this way, a trajectory contains fluid particle positions that are equally spaced in time for period  $\beta$ . They are also called temporal Poincaré sections and are obtained via

$$\mathbf{x}_{k+1} = \Psi(\mathbf{x}_k), \quad \mathbf{x}_k = \mathbf{x}(k\beta), \quad (7)$$

where  $\mathbf{x}_k$  is a particle position after  $k$  periods (i.e. time= $k\beta$ ).

In the Stokes limit trajectories of the PRHF are confined to spheroidal surfaces. While in Appendix E we give a formal proof of both the existence of a single invariant and that the motion on each spheroidal shell is Hamiltonian, the simplest way to see these results is to deform the hemisphere flow (formally via conformal transform) to that contained within a sphere. The reorientation step in the flow map is then a solid body rotation about the  $\hat{y}$  axis. The lid-driven shear is a non-uniform rotation about the  $\hat{x}$  axis. Composed rotations do not change the radius: the radius of every trajectory is invariant to the flow map (6), and every spherical surface at constant radius contains a family of trajectories confined to that surface. Reversing the conceptual conformal transform does not change the topology, it merely deforms the nested spherical surfaces into nested spheroids. Also in Appendix E we generalize this result to all lid-driven cavities by reducing the equations of motion to Hamiltonian-Poisson form.

## B. Symmetries

Symmetries of the base flow  $\mathbf{u}(\mathbf{x})$  are intimately tied to symmetries of Lagrangian trajectories and play an important role in the organization of the global 3D Lagrangian transport structure<sup>10,16,17</sup>. The base flow velocity field defines the trajectory of a fluid particle with initial condition  $\mathbf{x}(0) = \mathbf{x}_0$  via the kinematic equation

$$\frac{d\mathbf{x}}{dt} = \mathbf{u}(\mathbf{x}). \quad (8)$$

After a time  $t$ , the particle will have moved to  $\mathbf{x}(t)$  and this position can be written as the continuous flow map

$$\mathbf{x}(t) = \Phi_t(\mathbf{x}_0). \quad (9)$$

We introduce two maps  $S_x$  and  $S_z$  that reflect a particle position about  $x = 0$  and  $z = 0$ :

$$S_x : (x, y, z) \rightarrow (-x, y, z) \quad (10)$$

$$S_z : (x, y, z) \rightarrow (x, y, -z) \quad (11)$$

Fore-aft symmetry of the base flow (*i.e.* in the  $x$ -direction) results in a time-reversal symmetry,

$$\Phi_t = S_x \Phi_t^{-1} S_x, \quad (12)$$

Left-right symmetry of the base flow (*i.e.* in the  $z$ -direction) results in a reflection symmetry,

$$\Phi_t = S_z \Phi_t S_z, \quad (13)$$

So far, we discussed the symmetries of the base flow. We will discuss the symmetry of the reoriented flow in the following.

The time-periodic map  $\Psi$  has a time reversal symmetry that can be seen by substituting equation 12 (with  $t = \beta$ ) into equation 6:

$$\begin{aligned} \Psi &= R_{-\Theta} \Phi_\beta \\ &= R_{-\Theta} S_x \Phi_\beta^{-1} S_x \\ &= R_{-\Theta} S_x \Phi_\beta^{-1} R_{-\Theta}^{-1} R_{-\Theta} S_x \\ &= R_{-\Theta} S_x (R_{-\Theta} \Phi_\beta)^{-1} R_{-\Theta} S_x \\ &= R_{-\Theta} S_x \Psi^{-1} R_{-\Theta} S_x. \end{aligned}$$

Defining

$$R_{-\Theta} S_x = S_\Theta, \quad (14)$$

we then write  $\Psi$  as

$$\Psi = S_\Theta \Psi^{-1} S_\Theta. \quad (15)$$

This is the reversal-reflection symmetry of the map  $\Psi$ , where from equation 14  $S_\Theta$  is the map that reflects a particle about the plane  $\theta = \pi/2 - \Theta/2$  (figure 3). Defining the set of all the points on the plane  $\theta = \pi/2 - \Theta/2$  as  $\mathbf{I}_\Theta$ , it immediately follows that

$$\mathbf{I}_\Theta = S_\Theta \mathbf{I}_\Theta. \quad (16)$$

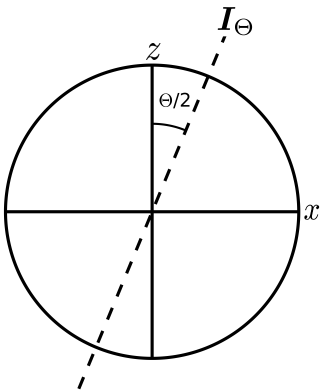


FIG. 3: Symmetry plane for  $\Theta = \pi/4$ .

All periodically reoriented flows have this symmetry, another example of which is the driven-lid cylinder, which has been extensively studied<sup>18–22</sup>.

The importance of the symmetry (equation 15) is twofold. First, P1 points (and by extension P1 lines) must lie on the symmetry plane  $I_\Theta$ . We prove this in Appendix C. Second, we only need to consider Lagrangian transport on one side of the symmetry plane  $I_\Theta$  because they will be mirrored across this plane.

The symmetry manifests as an invariant and the flow becomes an action-angle-angle system in canonical coordinates<sup>2,3</sup>. In action-angle-angle systems, isolated periodic points can not exist, only periodic lines with the ends attached to the boundary or closed periodic lines exist (see appendix B).

### C. Lagrangian Skeleton

In one invariant flows, as isolated periodic points cannot occur (see appendix B), periodic lines and their manifolds constitute all of the Lagrangian structure, and periodic lines may be called the Lagrangian skeleton of such flows. As generally, lower order periodic lines are more important in organising Lagrangian transport than higher-order periodic lines, P1 lines, being the most important of all, become the base of the Lagrangian skeleton of the PRHF system.

In the Stokes limit the PRHF has a single P1 line. In the limit  $\beta \rightarrow 0$  there is no flow, only rotation, and all trajectories are circular about the  $\hat{y}$  axis and the line between 0 and 1 on the  $\hat{y}$  axis is the sole P1 line. As  $\beta$  increases above zero this distinguished P1 line bends but remains anchored to the three non-trivial period-1 points (of which two are fixed points) for all values of  $\beta$  and  $\Theta$ . What are these three points? One is the centroid of the foliation of shells, which is a fixed point of the map for all  $(\beta, \Theta)$ ; such a central fixed point is generic for interior flows comprised of spheroidal shells. Another fixed point of the flow map is the point at the base of the hemisphere intersected by the  $y$ -axis. The third is an attachment point in the symmetry plane on the sliding lid that moves

from the center point of the lid at  $\beta = 0$  to the rim at  $\beta = 2 \sin(\Theta/2)$ , where it remains for  $\beta > 2 \sin(\Theta/2)$  due to the velocity discontinuity at this point. The path of the lid attachment point as  $\beta$  increases is elaborated in Appendix F.

Because this main P1 line approaches arbitrarily close to the boundary with increasing  $\beta$ , and all P1 lines must lie in the symmetry plane, it follows there are no other P1 lines attached to the boundary. A numerical search of the symmetry plane for closed loop P1 lines detected none of size greater than 0.4% of the hemisphere diameter. We conclude that for the Stokes PRHF there is only the single P1 line that runs from the apex of the hemisphere through the centroid to an attachment point on the lid or rim. Figure 4 shows for  $\Theta = \pi/4$  the sole P1 line in the symmetry plane for selected values of  $\beta$  from 0.1 to 15. Different values of  $\Theta$  do not qualitatively change the picture. In this figure, lines are coloured by the local character of the line: blue for elliptic regions and red for hyperbolic regions. Green dots are degenerate parabolic points, which play an important role in organizing transport, as we elaborate in section III.

From figure 4, it is seen that the tangent to a P1 line at the central stagnation point rotates anti-clockwise with increasing  $\beta$ . As  $\beta$  increases from 0, the end of the P1 line which is attached to the lid moves toward the hemisphere boundary and stops at the rim when  $\beta = 2 \sin(\Theta/2)$  (see Appendix F). Beyond this value of  $\beta$ , the P1 attachment point stays at the rim for all  $\beta$  values. The other end of the P1 line is fixed at the bottom of the hemisphere. Because both the ends of P1 lines are fixed for a given  $\beta$  and the tangent to the P1 line at the central stagnation point rotates anti-clockwise with increasing  $\beta$ , the length of P1 line increases with increasing  $\beta$ . As the rotation occurs at the central stagnation point, the P1 line is pushed towards the boundary.

### D. Summary of PRHF Lagrangian Structure

Due to the single invariant, PRHF consists of nested topological spheroids (or shells) that correspond to level sets of this invariant, each of which has a 2D Hamiltonian flow. Such 2D flows have been studied extensively, and the range of possible transport structures and their associated dynamics are well understood<sup>18–25</sup> (for example). Because the P1 line is constrained to lie entirely on the symmetry plane  $I_\Theta$  and passes from the hemisphere boundary to the lid boundary through the centroid of all the shells, it must pierce each shell at least twice. Where the P1 line intersects a shell, the Hamiltonian flow on that shell shares its local deformation character with the P1 line at that point.

Figure 5 shows an example of the P1 line, coloured by its deformation character as in figure 4, and views of several shells with Poincaré sections. The picture appears complicated with the only organizing principle being the sharing of deformation character where the P1

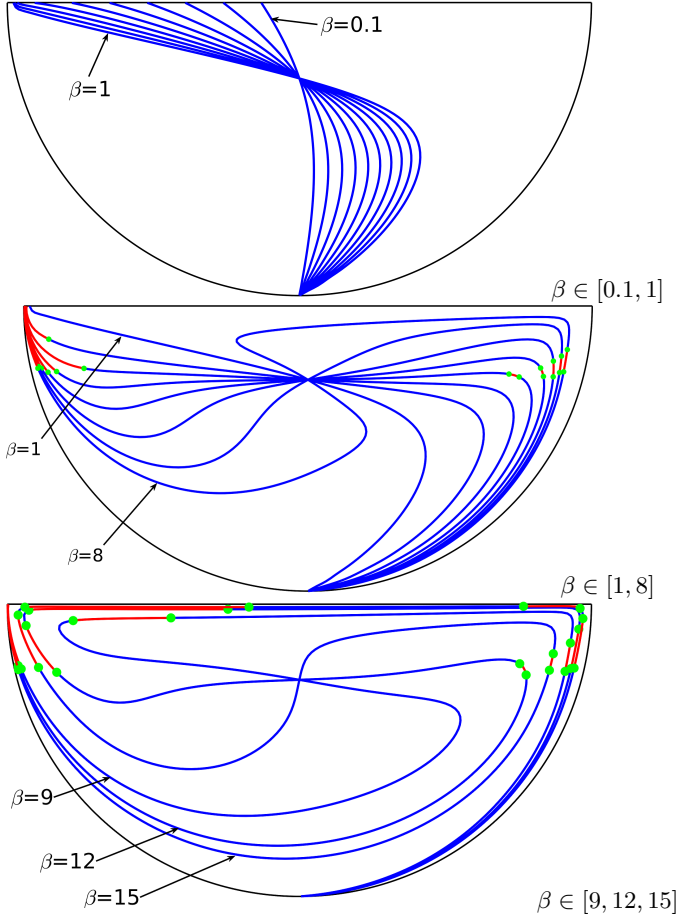


FIG. 4: P1 lines viewed perpendicular to the symmetry plane in normal space coordinates for  $\Theta = \pi/4$  and indicated values of  $\beta$ . Blue (red) are elliptic (hyperbolic) segments; green dots are degenerate parabolic points.

line pierces a shell. In the next section we show how the degenerate points along periodic lines determine the organizational skeleton of 3D Lagrangian transport in one-invariant volume-preserving flows.

### III. RESONANCES ON PERIODIC LINES

In bifurcation theory, the topology of a dynamical system changes as the parameter of the system goes through a bifurcation (or critical) point<sup>26</sup>. Analogously, in the PRHF, a type of bifurcation occurs when moving from one shell to another at degenerate points on periodic lines. Degenerate points have zero net deformation periodically. At such points, in the shell normal direction the local topology on adjacent shells changes and this behaviour can be viewed in terms of classical planar bifurcation theory by establishing an analogy between the PRHF and a 2D system with a parameter. Because fluid particles move on nested spheroids, these spheroids

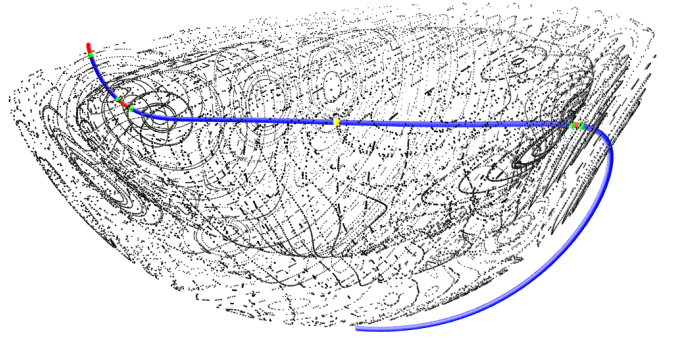


FIG. 5: P1 line and Poincare maps of flow on three shells. Oblique view.

can be considered as the direct product of a two dimensional phase space (angle variables  $\theta_1, \theta_2$ ) and a parameter space (action variable  $I$ , that we also call “shell number”). Conceptually the three-dimensional PRHF can be reduced to a two-dimensional system with a parameter  $I$ .

Importantly, deformation at degenerate points is constrained in such a way that zero net deformation in the neighbourhood of an  $n^{\text{th}}$  order degenerate point occurs after  $n$  periods. Degenerate points are called resonance points in classical planar bifurcation theory<sup>26</sup>. An  $n^{\text{th}}$  order degenerate point on a P1 line is termed a  $1:n$  resonance point. For example, a  $1:3$  resonance point is found on a P1 line and has zero net deformation in its neighbourhood after 3 periods. We can categorize resonant degenerate points as being of type  $m:p$  if they occur on a period- $m$  line and have an order  $p$ , (i.e. zero deformation after  $p$  periods), where  $p > m$  and  $p = n \times m$ , where  $n$  is a positive integer. Note that not every combination of  $m$  and  $p$  can occur because a point cannot simultaneously be a period- $m$  and period- $p$  point, e.g. resonances such as  $2:3$  can not occur.

The significance of a  $m:p$  resonance point does not lie chiefly in the zero net deformation in the neighbourhood of the point. We will show that the chief significance is that the constraints at degenerate points on periodic lines in 3D flows require the creation and coordination of extended spatial structures of period- $p$  lines that have specific sequences of elliptic and hyperbolic segments (each segment separated by another degenerate point). These in turn imprint specific Lagrangian structures onto sizeable 3D volumes of the fluid that extend well beyond the local neighbourhood of the degenerate point. It is found that, at degenerate points, lower order periodic lines and higher order periodic lines intersect. For example on a P1 line,  $n$  period- $n$  lines pass through a  $1:n$  resonance point except for  $1:1$  and  $1:2$  resonance points. At a  $1:1$  resonance, the P1 line is tangent to the invariant surface, and the degenerate nature of this point results in a cusp appearing in the Lagrangian structure on this shell. A period-2 line passes through a  $1:2$  resonance point on a P1 line. The reason only one period-2 line exists at a  $1:2$  res-

onance point instead of two period-2 lines is discussed in section III D. An analogy can be made between resonance points on a P1 line to resonance points on a higher order periodic line in the following way. A period- $m$  line of map  $\Psi$  can be considered as a P1 line of the map  $\Psi^m$ . This way, resonance points on the period- $m$  line are treated as resonance points on a period-1 line but with the map  $\Psi^m$ . In general, on a period- $m$  line,  $n$  ( $= p/m$ ) period- $p$  lines intersect at a  $m:p$  resonance point. This can be seen from the following: consider a 1:3 resonance point on a period-1 line. There will be three period-3 lines which intersect with the 1:3 resonance point. Again, consider a 3:9 resonance point on one of the three period-3 lines. There will be 3:9 resonance points similarly on the other two period-3 lines, totalling three 3:9 resonance points. Three period-9 lines pass through each of these 3:9 resonance points, totalling 9 period-9 lines which belong to the three 3:9 resonance points. These resonance bifurcations are local bifurcations in that they occur in the neighbourhood of periodic (or fixed) points.

Because the Lagrangian structure on a shell is completely determined by periodic line piercings, this hierarchical set of resonance points and accompanying periodic lines allows all the complicated structure exemplified in figure 5 to be uncovered in a systematic manner. This is undertaken in practice by finding the P1 lines and calculating the local and extended  $1:n$  structures, then finding the P2 lines and calculating the local and extended  $2:2n$  structures, etc., to whatever degree of detail is required.

The essentially 2D behaviour on invariant surfaces was noted as typical of periodic lines in<sup>18</sup> and<sup>22</sup> but the consequences of the degenerate points on global transport were not fully elaborated. Period-doubling and period-tripling bifurcations, which are associated with second order and third-order degenerate points, have also been observed<sup>25,27,28</sup>, but these studies did not explore the general  $m:p$  resonance structure. One of the novelties of the current paper is to systematically expose the set of possible structures.

Although resonance points can be identified on a periodic line of any order and used to calculate corresponding higher periodic lines, the analysis of resonance bifurcation points in this study is restricted mainly to P1 lines. In the rest of this section we first elaborate the effects of constraints on deformation on transport, then focus on the P1 line and give examples of the first four  $1:n$  spatially extended resonance structures. We also provide an example of a 2:6 resonance to demonstrate resonance points on higher-order periodic lines.

#### A. Constraints on Eigenvalues of the Deformation Tensor

Classification of periodic points by the eigenvalues of the deformation tensor is similar to the classification of critical points of a flow field<sup>30</sup>. Like all  $3 \times 3$  matrices, the deformation tensor  $\mathbf{F}$  has three matrix invariants: the trace  $\tau \equiv \text{tr}(\mathbf{F})$ ; second trace  $\sigma \equiv \frac{1}{2}(\text{tr}(\mathbf{F}^2) - \text{tr}^2(\mathbf{F}))$ ;

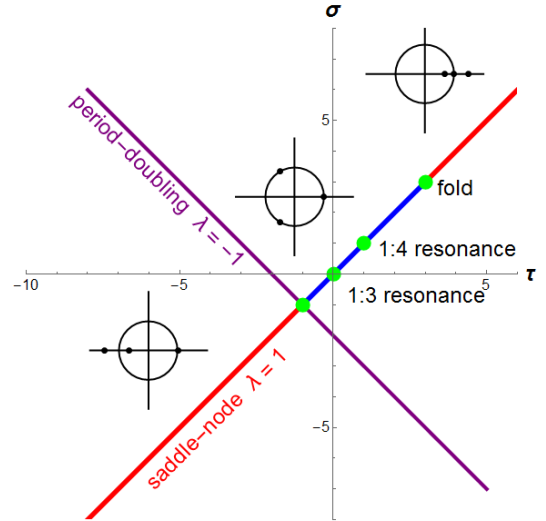


FIG. 6: Eigenvalues  $\lambda$  of the deformation tensor of a volume-preserving map plotted in terms of the trace  $\tau$  and second trace  $\sigma$  tensor invariants. As there is no deformation along any periodic line, one eigenvalue on every periodic line is one, and the other two eigenvalues lie along the diagonal line  $\sigma = \tau$ . The blue line segment denotes complex conjugate pairs—elliptic segments of the periodic line—and the red line segments denote real pairs—hyperbolic segments of the periodic line. Green dots locate the four strong resonances. The inset complex planes schematically depict the eigenvalues on the unit circle. Adapted from<sup>29</sup>.

and, determinant  $\det(\mathbf{F})$ . In terms of the invariants, the characteristic equation for the eigenvalues  $\lambda_i$  of  $\mathbf{F}$  is

$$\lambda^3 - \tau\lambda^2 + \sigma\lambda - \det(\mathbf{F}) = 0. \quad (17)$$

Volume-preservation constrains the deformation such that  $\det(\mathbf{F}) = \lambda_1\lambda_2\lambda_3 = 1$  everywhere in the flow. An additional constraint appears on periodic lines. Because each point on a period- $n$  line must return to the same point after  $n$  periods, there cannot be any deformation tangent to a periodic line, and thus one of the deformation eigenvalues must equal one on a periodic line. We define  $\lambda_3$  as the eigenvalue associated with the direction tangent to the periodic line, hence  $\lambda_3 = 1$  always, and  $\lambda_1, \lambda_2$  are associated with the directions tangent to the shell. This turns out to constrain the trace and the second trace to be equal on a periodic line (see Appendix D). Figure 6, adapted from Lomeli and Meiss<sup>29</sup>, is part of the general stability diagram for a volume-preserving map. Plotted in the  $(\tau, \sigma)$  parameter space, all eigenvalues of the deformation tensor on periodic lines correspond to points that lie on the line  $\tau = \sigma$ . In the blue part of the  $\tau = \sigma$  line, deformation near the periodic line is elliptic with rotation in closed orbits around the periodic line. The corresponding eigenvalues transverse to the periodic line's tangent direction appear as complex conjugate pairs of the form  $(e^{i\alpha}, e^{-i\alpha})$  and lie on the unit circle in the complex plane.

TABLE I: Resonances, their corresponding eigenvalues, and trace values on periodic lines;  $\lambda_3 = 1$  for each periodic point

Pm line ( $\Psi^m$ )	$m:m$ $m:2m$ $m:3m$ $m:4m$ ...
...	...
P2 line ( $\Psi^2$ )	$2:2$ $2:4$ $2:6$ $2:8$ ...
P1 line ( $\Psi$ )	$1:1$ $1:2$ $1:3$ $1:4$ ...
Trace	3 -1 0 1 ...
$\lambda_2$	1 -1 $-\frac{1}{2} - \frac{\sqrt{3}}{2}i$ ...
$\lambda_1$	1 -1 $-\frac{1}{2} + \frac{\sqrt{3}}{2}i$ ...
$\alpha$	0 $\pi$ $2\pi/3$ $\pi/2$ ...
	$2\pi/n$

In the two red parts of the  $\tau = \sigma$  line deformation near the periodic line is hyperbolic with a sheet stretching material away from the line in one direction and an equal amount of compression in a sheet towards the line. The corresponding eigenvalues transverse to the line's tangent direction are purely real and inverse to each other, i.e. of the form  $(\lambda, \lambda^{-1})$ .

At an  $n^{\text{th}}$  order degenerate point on the P1 line (a  $1:n$  resonance point),  $\mathbf{F}^n = I$ , which in turn implies  $\lambda_1^n = 1$ ,  $\lambda_2^n = 1$  and  $\lambda_3^n = 1$ . The eigenvalues of the deformation tensor at such a point are thus  $\lambda_3 = 1$  and  $\lambda_{1,2} = e^{\pm i(2\pi/n)}$ . The local rotation  $\alpha$  at the  $n^{\text{th}}$  order degenerate point is

$$\alpha = \frac{2\pi}{n}. \quad (18)$$

The trace of the deformation tensor  $\mathbf{F}$  at an  $n^{\text{th}}$  order degenerate point ( $\mathbf{x}_{1:n}$ ) is (via equation 19)

$$\tau(\mathbf{x}_{1:n}) = \text{Tr } \mathbf{F}(\mathbf{x}_{1:n}) = 1 + 2 \cos(2\pi/n). \quad (19)$$

Eigenvalues, the local rotation angle, and the trace of the deformation tensor for general  $m:p$  resonance points are given in table I.

Because the trace values of resonance points are known, we can identify these points by finding the roots of  $\tau(\mathbf{x}) - \tau(\mathbf{x}_{m:p}) = 0$ , where  $\mathbf{x}$  is a point on the periodic line and  $\mathbf{x}_{m:p}$  is a  $m:p$  resonance point. Once the resonance points are found, the corresponding higher order periodic lines can then be obtained using the method discussed in appendix A 3.

While there are an infinite number of resonances possible, corresponding to every root of unity, we will restrict our examination to the first four resonances (shown in figure 6), known classically from planar bifurcation theory as the “strong” resonances. As higher resonances, ( $n \geq 5$ ), are expected to have subharmonic bifurcation solutions only when exceptional conditions hold<sup>31</sup>, we focus on the cases ( $n \leq 4$ ) that will generically be encountered.

## B. Parameterization of Periodic Lines

To determine the fluid transport on a shell, it is necessary to first identify the periodic line piercings on the shell and their stability. These piercings are periodic points of the 2D flow on that shell. Even after calculating a periodic line numerically, it is difficult to infer how many times a periodic line pierces a particular shell. In order to more clearly identify this, we adopt the following approach. First, we define arc-length along a periodic line as the distance along the line from the bottom attachment point ( $r = 1, \theta = \pi/2, \phi = \pi/2$ ). Each point along the line thus has a unique value of arc length.

Then, we enumerate shell number at each point along the line arbitrarily in such way that shell number has a value of zero at the central fixed point and one on the lid and hemisphere boundaries. Shell number is a proxy for the action variable. Although this is not the only way to number shells, the choice makes no difference to the arguments that follow. Finally, the shell number versus arc length for the periodic line can be plotted, and the number of piercings of any shell is the number of times this curve crosses that shell number. In this plot, we also colour code the stability of each point (i.e. elliptic, hyperbolic or degenerate) along the line. As will be seen in the following sections, this will allow the number of piercings to be rapidly determined and will help in understanding global transport in this flow.

We now consider the structure associated with each of the strong resonances in turn.

## C. 1:1 Fold

A 1:1 resonance occurs in the flow at locations where  $\tau = 3$  on the periodic line and all three eigenvalues are one. As an example, the P1 line for  $\Theta = \pi/4$  and  $\beta = 16$  is shown in figure 7(a). Inside the box in this figure, two 1:1 resonance points occur, marked with green dots. Elliptic segments of the P1 line are marked in blue, and hyperbolic in red. As seen in the figure, the P1 line changes its characteristic from elliptic to hyperbolic (or *vice versa*) on opposite sides of a degenerate point. Additionally, the eigenvalues  $\lambda_1$  and  $\lambda_2$  change from complex to real (or real to complex) through  $\lambda_1 = \lambda_2 = 1$ . In appendix G we prove that extrema of P1 lines are always

tangent to shells and that the character of the line must change either side of an extremum.

The action and trace of the deformation tensor on the P1 line segment inside the box are plotted versus arc length in figure 7(b). The value of the trace is 3 at the two degenerate points. The corresponding points on the action versus arc length plot have zero slope (i.e. they are local extrema on this curve). This in turn means that the P1 line is tangent to an invariant shell at these points, and with respect to the action variable (shell number) the line literally folds here. In the language of planar catastrophe theory this point is called a fold bifurcation, whereas in 3D the line is literally folded.

The local Poincaré sections on shells containing the 1:1 resonance points inside the box in figure 7(a) are shown in figure 8 (with one shell in between). The normal coordinate has been stretched in order to more clearly see the effect of the 1:1 resonances. As seen, the P1 line is tangent to a shell at a 1:1 resonance point. The line goes from elliptic to hyperbolic through the first 1:1 resonance point and from hyperbolic to elliptic through the second. 1:1 resonance points observed in the PRHF always occur in pairs, and are connected through a hyperbolic segment. They always form a wiggly-like structure in action vs arc length plots as shown in figure 8. The character of the P1 line at piercing points is imprinted on the Poincaré sections. The upper and lower Poincaré sections contain a degenerate point and an elliptic point, and the middle section contains a hyperbolic point and two elliptic points. The stable and unstable manifolds of the hyperbolic point in the middle section have homoclinic orbits.

#### D. 1:2 Flip

At 1:2 resonance points, a period-2 (P2) line intersects the P1 line. The eigenvalues are  $\lambda_1 = \lambda_2 = -1$  and  $\lambda_3 = 1$ , and the local rotation angle is  $\pi$ . The net deformation at a 1:2 resonance point is zero after two periods. The stability of period-1 points on the P1 line changes at the 1:2 resonance point from elliptic to hyperbolic (or *vice versa*), and the eigenvalues  $(\lambda_1, \lambda_2)$  change from complex to real negative (or real negative to complex).

As an example, the P1 line on the symmetry plane for the case  $\Theta = \pi/8$  and  $\beta = 2$  is shown in figure 9(a). The action and trace versus arc length are shown in figure 9(b). In this figure, the single 1:2 degenerate point is coloured green and has a trace value of  $-1$  (see table I). The change of stability of P1 at a 1:2 degenerate point is also seen in figure 9(b) in the change from blue (elliptic) to red (hyperbolic).

The period-2 line which goes through the 1:2 resonance point is computed numerically using the method discussed in appendix A3 and a perspective view is in figure 10. The action value along P1 and P2 is plotted against arc length in figure 11 where here, arc length is shifted to have its origin at the 1:2 resonance point.

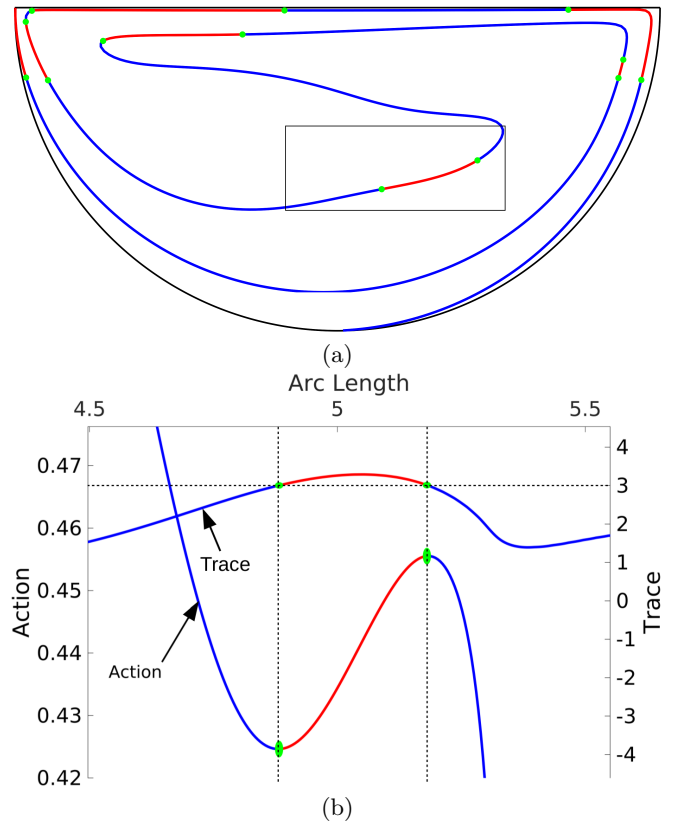


FIG. 7: (a) P1 line in the symmetry plane for  $(\beta, \Theta) = (16, \pi/4)$ . Red (blue) is hyperbolic (elliptic) line segment. (b) The action and trace values versus Arc length of points on the P1 line inside the rectangular box in (a)

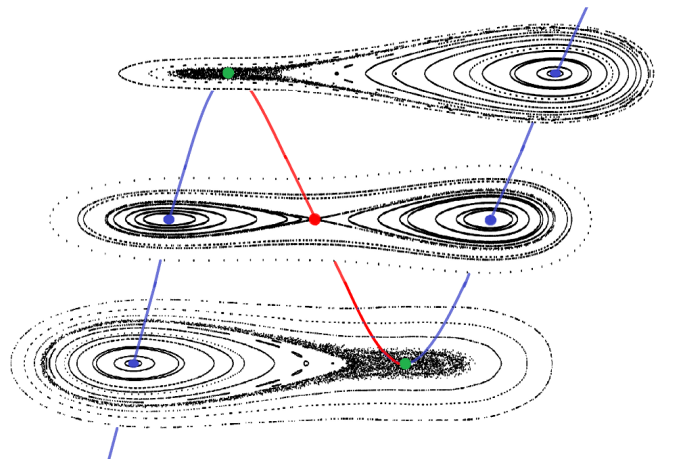


FIG. 8: A close up of the P1 line in the rectangular box in figure 7(a) with local Poincaré sections superposed. The upper and lower sections are shells with degenerate points that coincide with cusps in the sections. The middle section is on a shell half way between. For clarity the shell-normal coordinate is expanded.

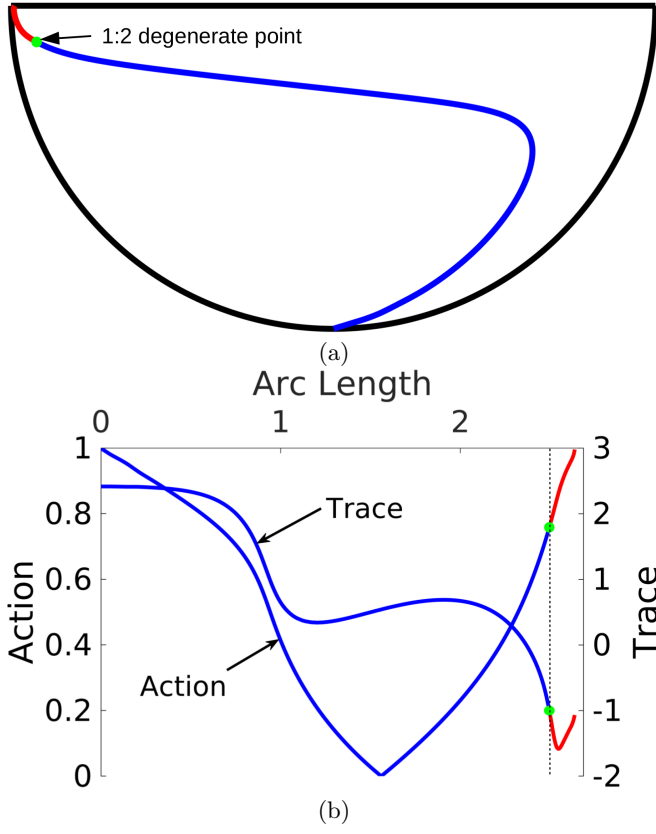


FIG. 9: (a) The P1 line for  $\beta = 2$  and  $\Theta = \pi/4$  on the symmetry plane. (b) Action and trace versus arc length on P1.

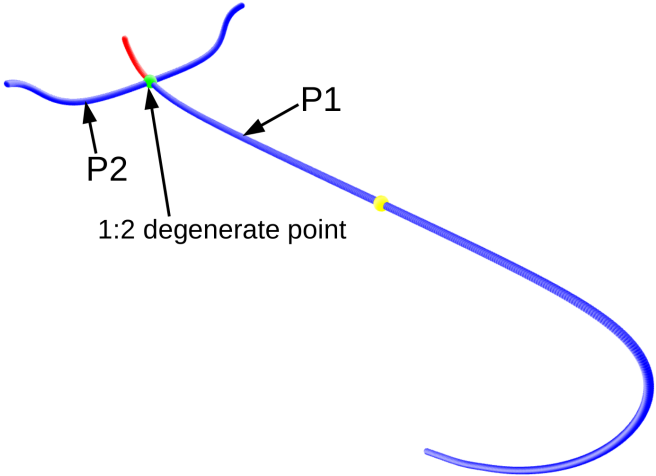


FIG. 10: P1 and P2 lines for  $\beta = 2$  and  $\Theta = \pi/4$

From figures 10 and 11, we observe that the period-2 line is symmetric about the symmetry plane and its ends are attached to opposite sides of the hemisphere boundary. Local Poincaré sections on a shell containing the 1:2 resonance point and a neighbouring shell are shown in figure 12. Again, the shell-normal coordinate is stretched to highlight the key features of the Lagrangian structures.

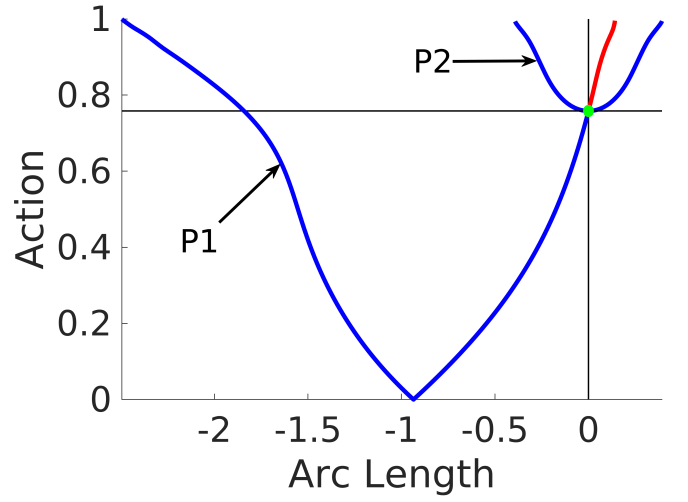


FIG. 11: Action vs arc length of P1 and P2 lines for  $\beta = 2$  and  $\Theta = \pi/4$

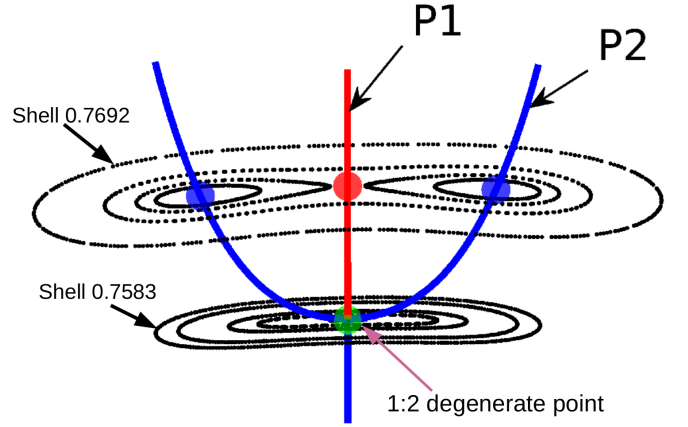


FIG. 12: 3-dimensional 1:2 resonance structure; period-doubling bifurcation in space with the action or shell number as the bifurcation parameter. Blue is elliptic, red hyperbolic, and green degenerate. The symmetry plane is normal to the page along the P1 line. The period-2 elliptic lines are symmetric about the symmetry plane.

The lower section (action  $I = 0.7583$ ) contains the 1:2 degenerate point and the upper section (action  $I = 0.7692$ ) contains one period-1 hyperbolic point and two period-2 elliptic points. All piercings on sections are shown with solid spheres, blue for elliptic, red for hyperbolic points, and green for degenerate. The stable and unstable manifolds of the hyperbolic point on P1 have homoclinic orbits as seen in figure 12.

The reason a single period-2 line passes through a second order degenerate point instead of two period-2 lines is the following. Because eigenvalues of the deformation tensor at degenerate points of order  $n \geq 3$  are complex as shown in table I and the eigenvalues change continuously along the P1, the P1 line character does not change at

these degenerate points and remains as elliptic. For example, the P1 line character changes at the 1:2 resonance point (see figure 12), where as at 1:3 and 1:4 resonance points the P1 line character does not change (see figures 16 and 19). In general, a chain of  $n$  period- $n$  elliptic islands appear on an invariant surface in the neighbourhood of an  $n^{\text{th}}$  order degenerate point and the centres of these islands are period- $n$  elliptic points, as shown in the upper sections of figures 12, 16 and 19. The chain of  $n$  elliptic islands are connected by the manifolds of  $n$  period- $n$  hyperbolic points for  $n \geq 3$ , forming heteroclinic connections (e.g. see the upper sections of figures 16 and 19). In contrast, at a second order degenerate point, the two elliptic islands are connected by manifolds of a hyperbolic period-1 point instead of two period-2 hyperbolic points as shown in the figure 12, forming a homoclinic connection. Because of the existence of this hyperbolic period-1 point which is due the P1 line character change at the 1:2 degenerate point, two additional hyperbolic period-2 points are not possible to connect the islands. Hence there is only one period-2 line which passes through the 1:2 degenerate point.

### E. 1:3

At a 1:3 resonance point, three period-3 lines ( $P3_1, P3_2$  and  $P3_3$ ) intersect P1. The local rotation angle is  $2\pi/3$  and the deformation tensor has eigenvalues  $\lambda_{1,2} = e^{(\pm i2\pi/3)}$ ,  $\lambda_3 = 1$ . The net deformation at the resonance point is zero after 3 periods. The properties of a 1:3 resonance point are described using an example with  $\Theta = \pi/8$  and  $\beta = 1$ . The P1 line lies in the symmetry plane and is shown in figure 13(a), where it is seen in the inset that 1:2, 1:3 and 1:4 resonance points exist on P1 in close proximity to each other. In this section we consider only the 1:3 resonance.

Action and trace values of the deformation tensor on the P1 line are shown in figure 13(b) where the trace value of 0 corresponds to the 1:3 resonance point (see table I). A perspective view of P1 and the three period-3 ( $P3$ ) lines are shown in figure 14. Action values on P1 and the three  $P3$  lines are plotted against arc lengths in figure 15(a) where  $P3$  arc length is redefined with an origin at the 1:3 resonance point. A close-up of the rectangular box in figure 15(a) is shown in figure 15(b). P1 and  $P3_1$  lie in the symmetry plane, and from figure 15(b) and figure 14, it is observed that, all period-3 line ends are attached to the hemisphere boundary.  $P3_2$  and  $P3_3$  are reflections of each other across the symmetry plane, and can be defined by  $P3_3 = S_\Theta P3_2$ .

The local Poincaré sections on a shell containing the 1:3 resonance point and two neighbouring shells (one below, one above) are shown in figure 16. The shell-normal coordinate is stretched for clarity. Each of the  $P3$  lines has an extremum on the lower shell (action value 0.8607), i.e. the three period-3 lines are all tangent to this same shell. This is seen in the tri-cuspid structure with a cen-

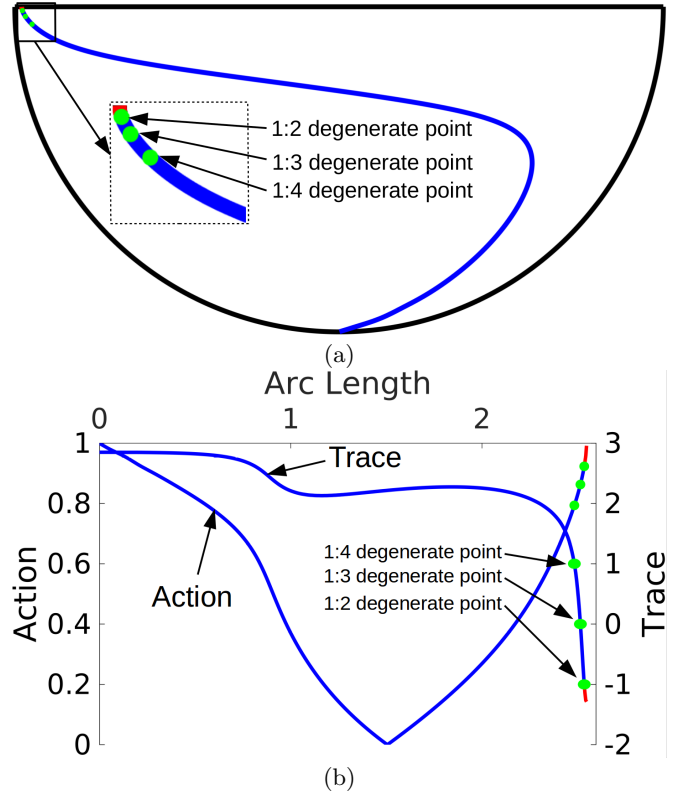


FIG. 13: (a) P1 line for  $\beta = 1$  and  $\Theta = \pi/8$  on the symmetry plane. (b) Action and trace along P1.

tral period-1 elliptic point. The middle section (action value 0.8628) contains three period-3 elliptic points and the 1:3 resonance point through which P1 and all period-3 lines pass (by definition). The upper section (action value 0.8649) contains three period-3 elliptic points, three period-3 hyperbolic points, and a period-1 elliptic point. All piercings on the Poincaré sections are shown with solid spheres. The stable and unstable manifolds of the period-3 hyperbolic points on the upper section have heteroclinic connections which create four connected islands, which act as transport barriers.<sup>25</sup> gave a detailed analysis of a 1:3 resonance; a notable feature is that the sense of rotation along the P1 line reverses either side of the degenerate point.

### F. 1:4

At a 1:4 resonance point, four period-4 lines intersect P1. The eigenvalues of the 1:4 resonance are  $\lambda_{1,2} = e^{(\pm i2\pi/4)}$ ,  $\lambda_3 = 1$  (and  $\text{Tr} = 1$ ). The net deformation is zero after four periods, and the local rotation angle is  $\pi/2$ . We use the same parameters ( $\Theta = \pi/8$  and  $\beta = 1$ ) here as in the previous section to discuss the case in figure 13(b) with trace = 1 which is the 1:4 resonance point. This point is also shown on the P1 line in figure 13(a). P1 and the four period-4 lines ( $P4_1$ - $P4_4$ ) are shown in per-

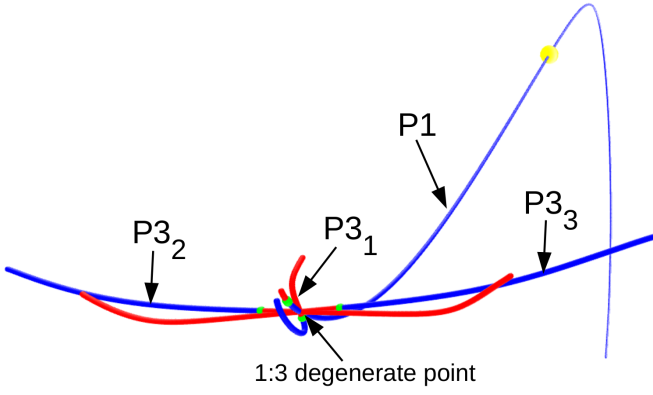


FIG. 14: P1 and P3 lines for  $\beta = 1$  and  $\Theta = \pi/8$

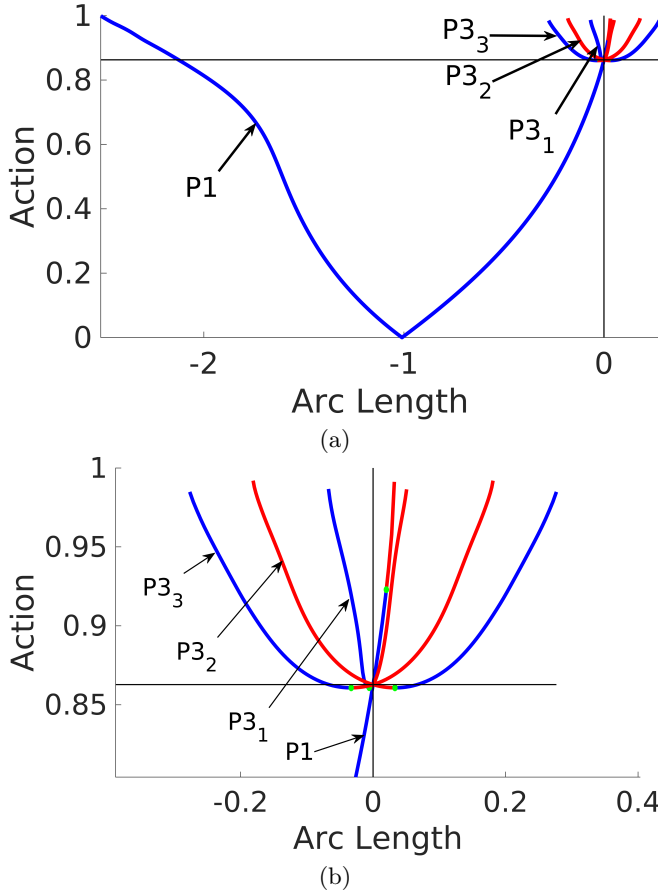


FIG. 15: (a) Action is plotted along P1 and P3 lines for  $\Theta = \pi/8$  and  $\beta = 1$  (b) Top right segment of figure (a).

spective in figure 17. The action value of all lines plotted against arc length are shown in figure 18(a), where again, arc length is redefined with its origin at the 1:4 resonance point.

A close-up of the rectangular box in figure 18(a) is shown in figure 18(b). Perhaps not obvious from figure 17 and figure 18(b), is that  $P_{41}$  and  $P_{44}$  lie on the symmetry plane, and that  $P_{43}$  and  $P_{42}$  are reflections of each other about the symmetry plane and are related by  $P_{43} =$

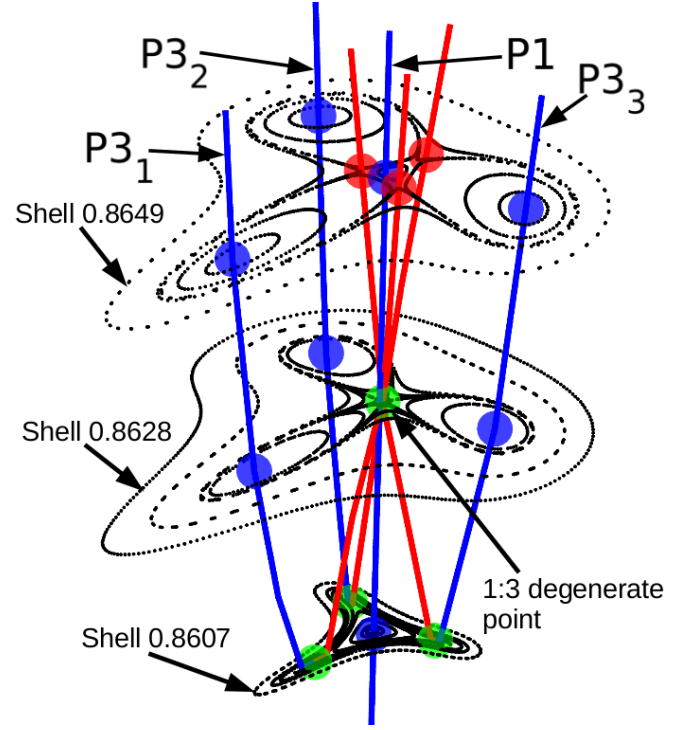


FIG. 16: 3-dimensional 1:3 resonance structure. Blue is elliptic, red hyperbolic, and green degenerate. Left is a 3-dimensional view of selected shells, exploded along the tangent direction of the P1 line. Right are planar projections of the shells. Period tripling bifurcation in space with the action or shell number as the bifurcation parameter.

$S_{\Theta}P_{42}$ . All four P4 lines are attached to the hemisphere boundary at both ends.

The local Poincaré sections on the shell containing this 1:4 resonance point and a shell above is shown in figure 19. The lower section (action value 0.7935) contains the 1:4 degenerate point and the upper section (action value 0.7976) contains the four period-4 elliptic points, four period-4 hyperbolic points and one P1 elliptic point. All the piercings sites on a Poincaré section are shown with solid spheres. The stable and unstable manifolds of the period-4 hyperbolic points on upper section have heteroclinic connections. The heteroclinic connections create five islands (four period-4 islands and one period-1 island), and these islands act as transport barriers.

### G. Hierarchy of Resonances: a 2:6 example

One of the main findings of this study is that resonance points, coordinating lower-order periodic lines and higher-order periodic lines, act as nodes in the Lagrangian network of periodic lines in one invariant flows. These resonance points organise periodic lines, which then controls fluid transport. Resonances on P1 lines are discussed so far. To demonstrate the organisation

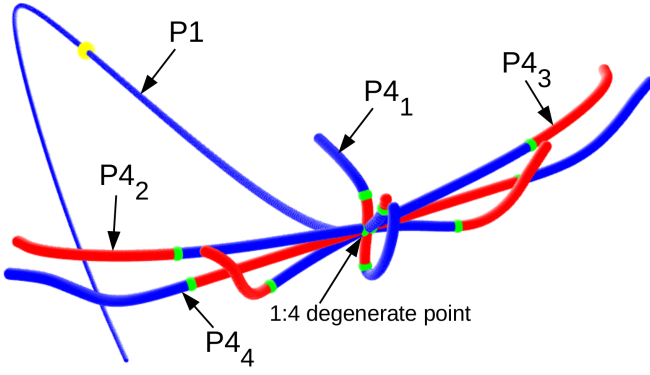
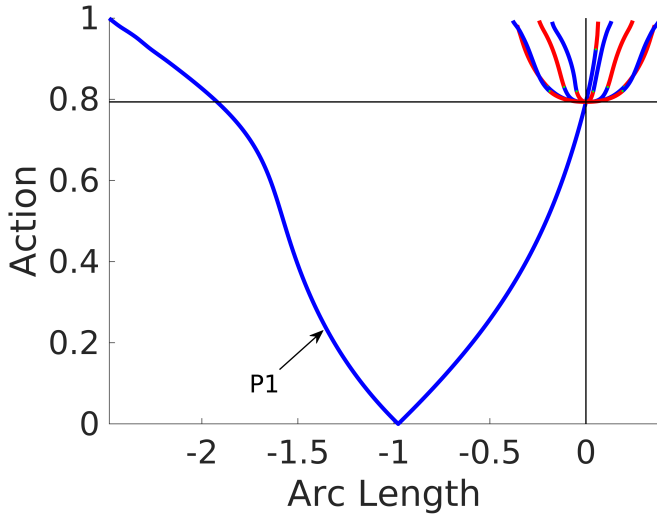
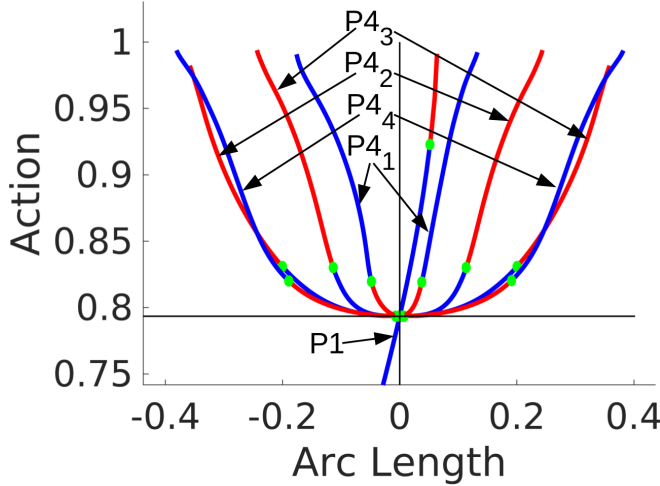


FIG. 17: P1 and P4 lines for  $\beta = 1$  and  $\Theta = \pi/8$



(a)



(b)

FIG. 18: (a) Action is plotted along P1 and P4 lines for  $\Theta = \pi/8$  and  $\beta = 1$  (b) Top right segment of figure (a)

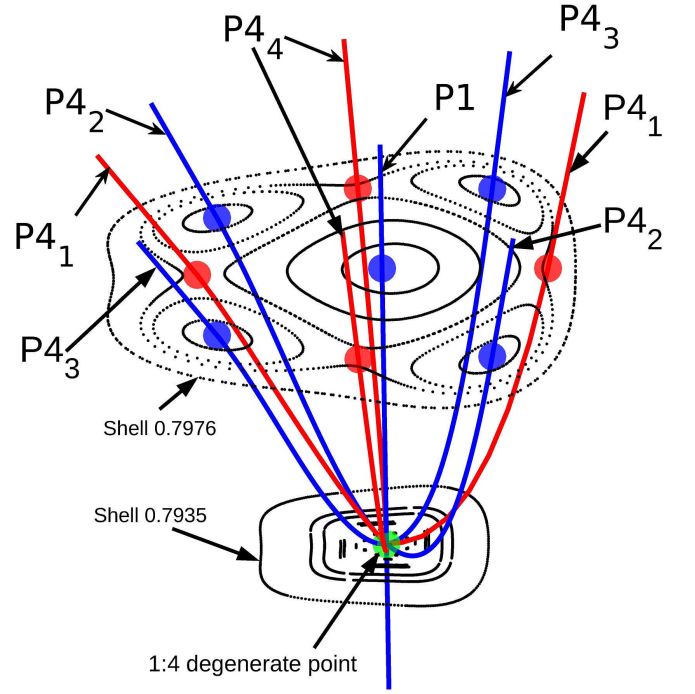


FIG. 19: 3-dimensional 1:4 resonance structure. Blue is elliptic, red hyperbolic, and green degenerate. A 3-dimensional view of selected shells, exploded along the tangent direction of the P1 line. Bifurcation in space with the action or shell number as the bifurcation parameter.

of periodic lines by resonances on higher-order periodic lines, a 2:6 resonance is described with the example of  $\Theta = \pi/4$  and  $\beta = 2$ , which is the same example used in section IIID to describe 1:2 resonance. A 1:2 resonance point is identified on the P1 line of  $\Theta = \pi/4$  and  $\beta = 2$ , and the period-2 line which passes through the 1:2 resonance point is calculated. On this period-2 line, 2:6 resonance points are identified, and the corresponding period-6 lines which pass through them are calculated numerically using the method discussed in appendix A 3. The 2:6 resonance points and their associated higher-order periodic lines are shown in figure 20. In this figure, a period-2 line (P2) intersects the period-1 line (P1) at the 1:2 resonance point and three period-6 lines ( $P_{6_1}$ ,  $P_{6_2}$  and  $P_{6_3}$ ) intersect the period-2 line at the 2:6 resonance point. In this figure, there is a symmetric structure on the other side of the P2 line (due to the symmetry in the PRHF), however, for clarity only the 2:6 resonance point, not the P6 lines, is shown.

Following this approach, the detailed Lagrangian skeleton of a one-invariant flow can be calculated systematically, by first identifying resonance points on P1 lines and calculating their corresponding higher-order periodic lines, next identifying resonance points on P2 lines and calculating their corresponding higher-order periodic lines. This process is continued recursively until enough Lagrangian structure detail is obtained for any given pur-

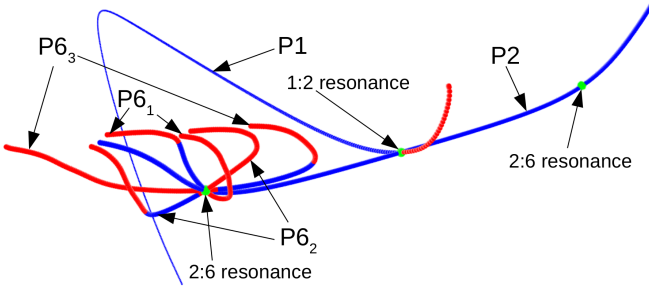


FIG. 20: A period-1 line (P1), a period-2 line (P2) and three period-6 lines ( $P6_1$ ,  $P6_2$  and  $P6_3$ ) coordinating via 1:2 resonance point and 2:6 resonance points for  $\Theta = \pi/4$  and  $\beta = 2$ .

pose, e.g. those in figure 5.

### H. Global Bifurcations

In the examples of resonances discussed so far, higher order periodic lines extend from the resonance points and terminate on the hemisphere boundary. However it is also possible that a higher order periodic line from one resonance point can connect with another resonance point of the same order within the fluid bulk. In this way, the line forms a truly global Lagrangian structure.

An example where such structures arise occurs in the flow with  $\Theta = \pi/8$  and  $\beta = 4$ . The P1 line is shown in figure 21(a) and the action and trace as functions of arc length along P1 are shown in figure 21(b). Although a little difficult to discern in figure 21(b), the trace has five points with value -1, corresponding to five 1:2 resonance points along P1. Each of these points lie on different shells and are labelled from 1-5 with increasing arc length. The P2 Line connected to point 5 attaches to the hemisphere wall like the P2 line seen previously in figure 10, whereas the first four 1:2 resonance points have different behaviour.

The period-2 lines corresponding to these four points are shown in figure 22, where the period-2 lines extending from resonance points 1 and 3 join together to form a single closed period-2 line ( $P2_1$ ) that lies in the symmetry plane, recalling that the P1 line marks the symmetry plane. The period-2 lines extending from resonance points 2 and 4 also join together to form a single closed period-2 line ( $P2_2$ ) that extends in an almost normal direction to the symmetry plane. These two closed P2 loops are interlinked.

The P1 and P2 lines impart their character locally on shells at the piercing points and the looped nature of these closed curves coordinates the behaviour of the 2D surface flow at distant points on a shell. Action values on the P1 and P2 lines are plotted against arc length in figure 23. Since the period-2 lines here are closed, arc length values for them are calculated from arbitrary starting points on the lines. To examine influence of the

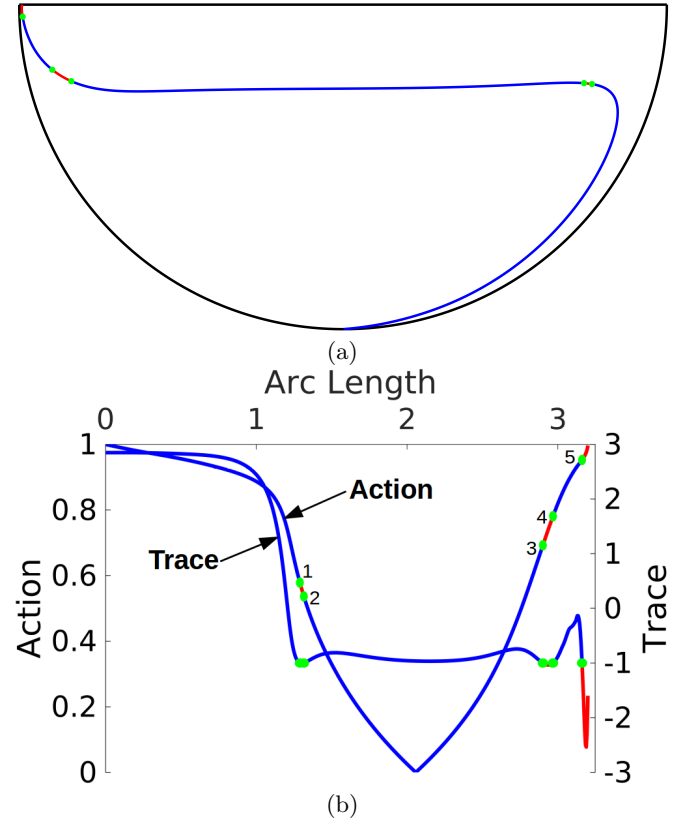


FIG. 21: (a) P1 line for  $\beta = 4$  and  $\Theta = \pi/8$  on symmetry plane. (b) Action and trace along P1

period-2 lines on the Lagrangian behaviour of the shells, three nearby shells (shell values 0.5285, 0.5588 and 0.5919) are considered (shown as the three horizontal black lines in figure 23).

#### Shell 0.5285

The Poincaré section on shell 0.5285 is shown in figure 24 and includes P1 and both period-2 lines. Periodic line piercing points are highlighted with a small solid sphere and are labelled 1 to 10 for reference. The shells are made translucent so that periodic line segments inside and outside of the shell can be distinguished. Lines and spheres are coloured blue for elliptic and red for hyperbolic. Figure 24(a) presents the view from the bottom of the hemisphere, (b) presents the view from the side and a little above the shell and (c) presents a flattened out view of the section projected onto a 2D sheet. As most clearly seen in figure 24(c), shell 0.5285 contains four period-2 elliptic points, four period-2 hyperbolic points and two period-1 elliptic points. The stable and unstable manifolds of the four period-2 hyperbolic points have heteroclinic connections.

#### Shell 0.5588

As shell number increases (i.e. we move further away from the central stagnation point), two of the hyperbolic

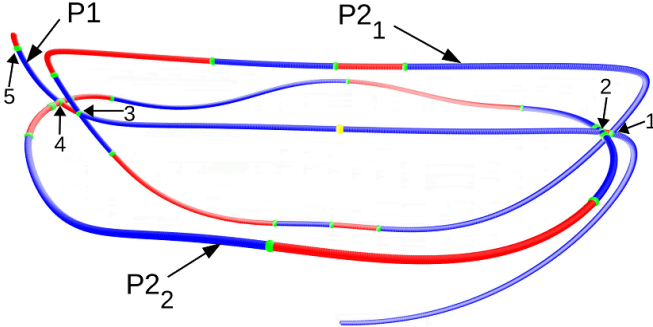


FIG. 22:  $\Theta = \pi/8$  and  $\beta = 4$ , Period-1 line  $P1$  and period-2 line  $P2_1$  are on symmetry plane, and period-2 line  $P2_2$  is symmetric about symmetry plane. Elliptic line segments are coloured blue, hyperbolic line segments are coloured red and degenerate points are coloured green. The first four 1 : 2 resonance points on  $P1$  are also shown with numbers 1 – 4.

piercing points on  $P2_2$  disappear (as the corresponding segment of the  $P2$  line no longer pierces this shell which fully contains 1:2 resonance point number 2). The character of  $P1$  also changes from elliptic to hyperbolic. Similar plots of the Poincaré section on shell 0.5288 are shown in figure 25. This shell now contains four period-2 elliptic points, two period-2 hyperbolic points, a period-1 elliptic point and a period-1 hyperbolic point. The stable and unstable manifolds of two period-2 hyperbolic points have heteroclinic connections. The stable and unstable manifolds of the period-1 hyperbolic point have homoclinic connections.

#### Shell 0.5919

As shell number increases further to 0.5919, 1:2 resonance point number 1 now falls inside this shell and the  $P2$  lines no longer pierce it in the vicinity of  $P1$ . Thus two period-2 elliptic points disappear and the hyperbolic  $P1$  line becomes elliptic once more. Similar plots of the Poincaré section for shell 0.5919 are shown in figure 26. The shell contains two period-2 elliptic points, two period-2 hyperbolic points and two period-1 elliptic points. The stable and unstable manifolds of two period-2 hyperbolic points have heteroclinic connections.

If shell number was increased still further, 1:2 resonance point 3 would cease to impart its structure locally on the Poincaré sections and eventually 1:2 resonance point 4 would follow suit. The most important point to come out of the results presented in this section is that global and connected Lagrangian structures can be born from resonance points along the  $P1$  line. Although we do not explicitly show it here, similar statements can be made regarding higher order resonances that rise on higher order periodic lines.

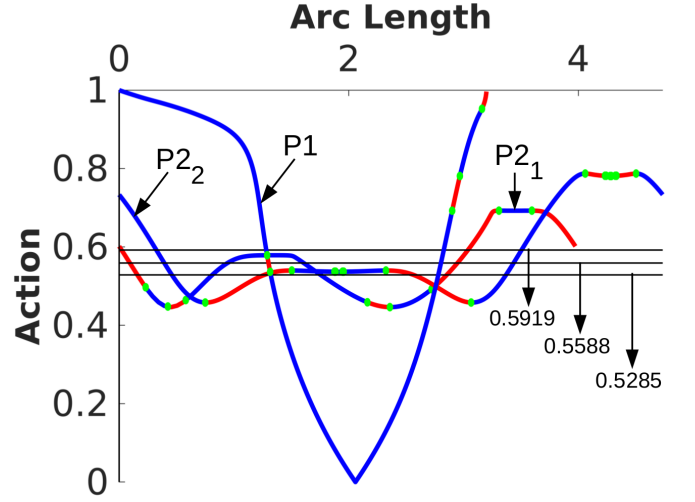


FIG. 23: Action versus arc length along periodic lines ( $P1$ ,  $P2_1$  and  $P2_2$ ) shown in figure 22 are shown. Three lines which correspond to action values (0.5285, 0.5588, 0.5919) are also shown.

#### IV. CONCLUSIONS AND DISCUSSION

In this paper we considered the Periodically Reoriented Hemisphere Flow (PRHF), an example of an 1-invariant flow which consists of a set of nested, topologically spherical, space-filling shells on which all transport occurs. In one invariant flows, isolated periodic points cannot exist (see Appendix B); closed periodic lines or periodic lines with ends attached to the boundary are possible. In the Stokes PRHF, a single  $P1$  line exists on the symmetry plane for all parameter values and forms the basis of the Lagrangian skeleton of the flow. This  $P1$  line connects three non-trivial fixed points: a point at the bottom of the hemisphere; a central stagnation point which is at the centre of the topological spheres; and, a point on the lid.

We define shell number as a unique (continuous) variable that acts as a proxy for the action variable (in an action-angle-angle coordinate system). By plotting shell number as a function of distance along  $P1$ , the local Lagrangian topology generated by the periodic lines can be quickly and simply determined based solely on the number of shell piercings and their character. Although demonstrated here for the PRHF, this same methodology can be used for any similar 1-invariant system in which the action variable can be quantified in some way. This then allows a global understanding to be quickly and simply obtained of the likely types of Lagrangian structure on different invariant surfaces of the flow.

Using this approach on the PRHF allowed us to show that the  $P1$  line passes through each shell at least twice. Wherever  $P1$  pierces a shell, the stability of the piercing period-1 point is imparted to the 2D transport on that shell in the neighbourhood of the piercing site. In the limit  $\beta \rightarrow 0$ , the  $P1$  line is a stagnation line that coincides

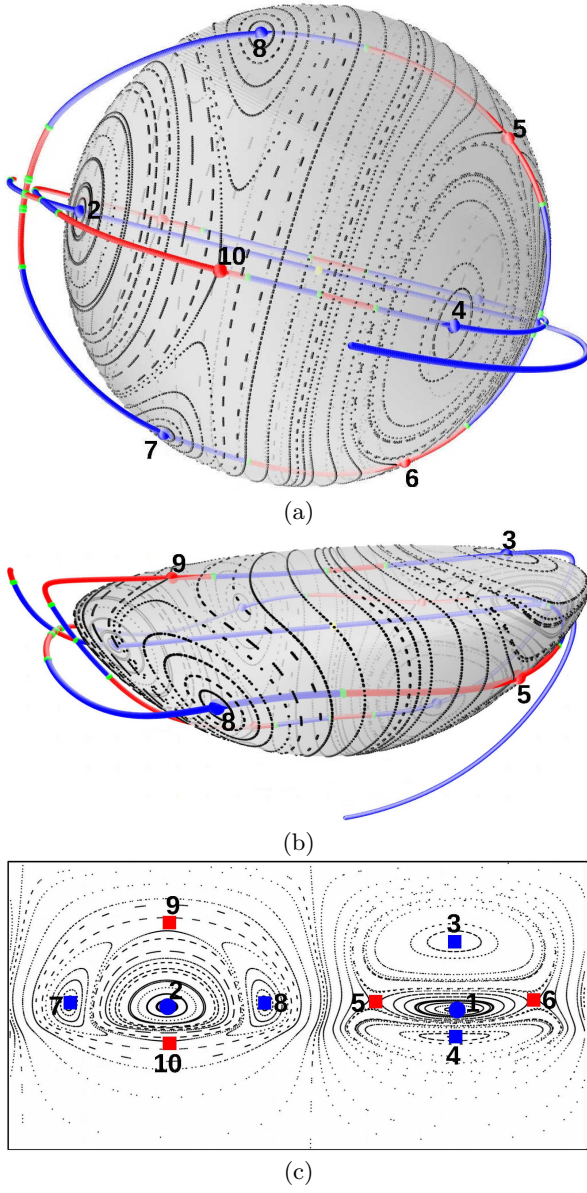


FIG. 24: The periodic lines shown in figure 22 impart their character on to shell 0.5285; Stroboscopic map on Shell seen from (a) Bottom (b) Side and above (c) Stroboscopic map projected on to a plane. P1 piercing points are represented by circles and P2 piercing points represented by squares; blue for elliptic and red for hyperbolic.

with the  $y$  axis. As  $\beta$  increases, the tangent to the P1 line at the central stagnation point rotates anti-clockwise which increases the total length of the P1 line (since both the ends of a P1 line are fixed). For very low  $\beta$  values, the entire P1 line is elliptic and pierces each invariant surface only twice. As  $\beta$  increases from very low to low values, hyperbolic segments start appearing on the P1 line, although it still pierces each invariant surface only twice.

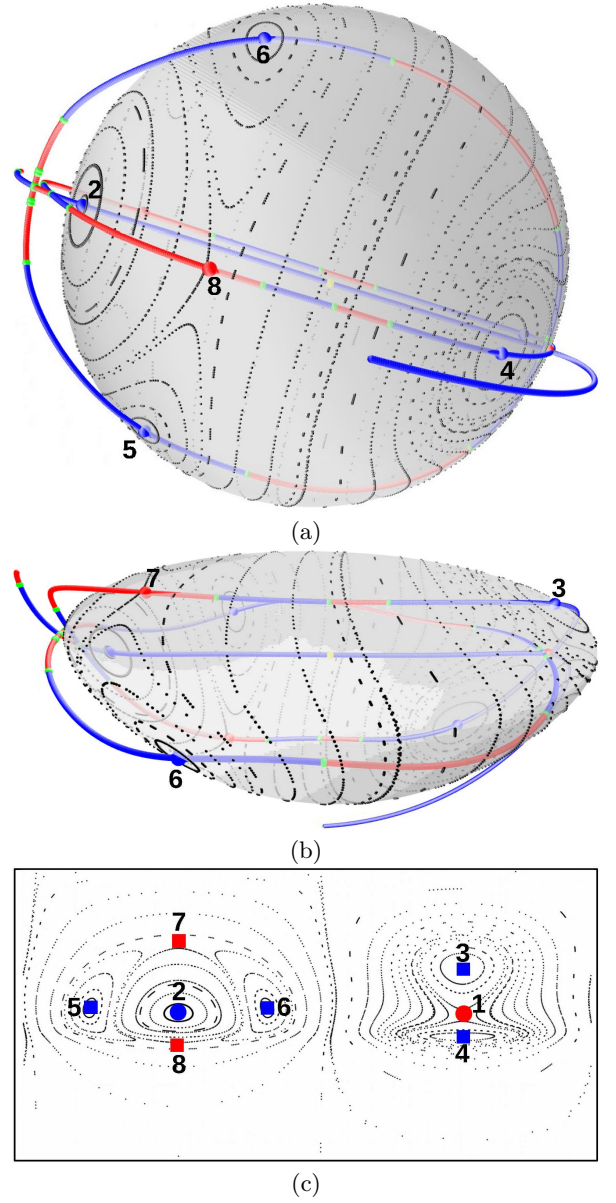


FIG. 25: Poincaré sections on shell 0.5588. See caption for figure 24 for details

As  $\beta$  increases further, the P1 line starts folding inside a shell it has already pierced. The tangent point delineates a change of periodic character on P1 from elliptic to hyperbolic (or *vice versa*) and an increase (or decrease) by two in the number of period-1 points on shells just inside and outside of the degenerate shell. This leads to the creation of two local extrema (one minimum, one maximum) which constitute a wiggle in the action vs arc length plot. Each local extrema in the wiggle correspond to a point at which the P1 line is tangent to a shell and each is also a first-order degenerate point which corresponds with a cusp on the shell's 2D Poincaré section. A single wiggle accommodates two first order degenerate points, and the P1 line segment between these degener-

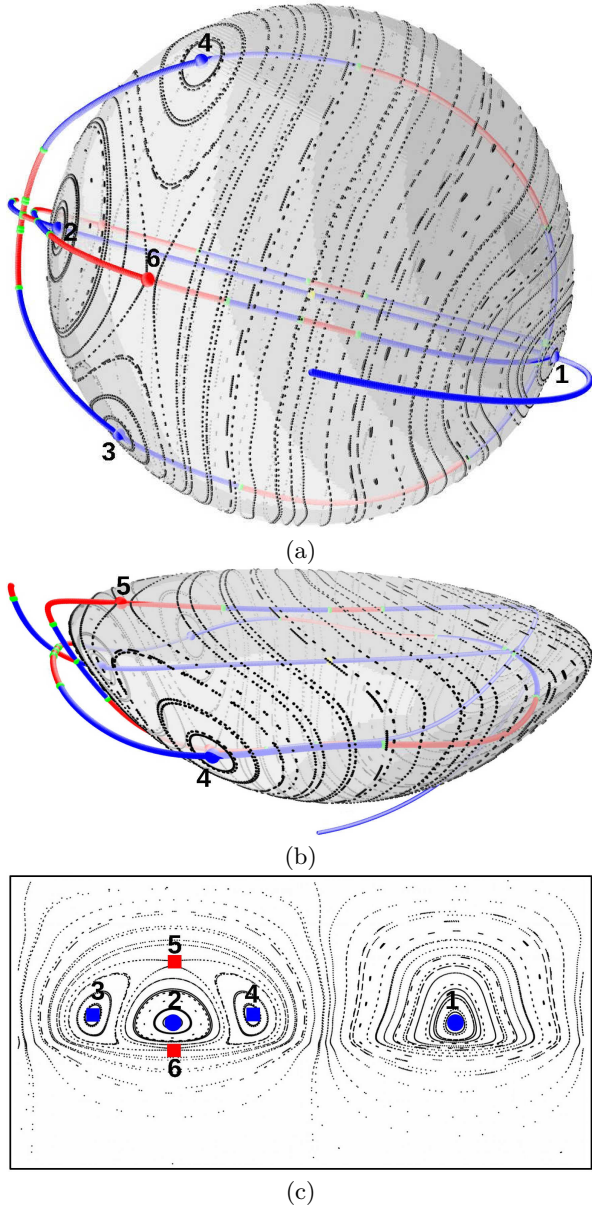


FIG. 26: Poincaré sections on shell 0.5919. See caption for figure 24 for details

ate points is always of hyperbolic type, with both sides of the P1 line segments being elliptic.

The degenerate points on periodic lines are analogous to fixed point resonances in classical planar bifurcation theory. At an  $n^{\text{th}}$  order degenerate point on a P1 line (also called a 1- $n$  resonance point),  $n$  period- $n$  lines intersect the P1 line except for the cases of  $n = 1$  and 2. The resonance points on a periodic line can be easily identified by calculating the trace of the deformation tensor value along the periodic line. Resonance points have unique trace values as specified in table I. At a first order degenerate point, the P1 line is tangent to one of the shells. At a second order degenerate point (a 1:2 resonance), a period-2 line intersects the periodic-

1 line. A higher-order periodic line intersecting with a lower order periodic line at a resonance point can be calculated numerically by identifying the resonance point using the method discussed in appendix A 3. The significance of these resonances points is that one action flows can be completely understood by finding the resonance points on the P1 lines first, and then computing the corresponding higher-order periodic lines. Then period-2 lines can be computed, resonance points located, then determine the corresponding higher-order periodic lines, and so on. This process is pursued recursively until enough Lagrangian transport structures are uncovered for any given purpose.

A higher-order periodic line extending from a resonance point may attach to the boundary, or higher-order periodic lines extending from different resonance points can sometimes join together to form a closed periodic line. These resonance bifurcations are local bifurcations because they can be found in the neighbourhood of periodic points (or fixed points). The Lagrangian structures emanating from different resonance bifurcation points can sometimes connect with each other and form truly global transport structures. With this way of building extended structures from lower order to higher order periodic lines, truly global Lagrangian transport structures can be uncovered for any one action flow.

In work still to be published, we introduce inertia to the flow to break the remaining symmetry and perturb the Stokes resonance structures. We will see that the resonance structures identified in this paper are perturbed into 3D Lagrangian coherent structures that appear to be generic in the sense that they depend on starting from a specific Stokes resonance and not on specific values of parameters. An experiment is under construction that will allow these structures to be visualised in a flow and will be reported in due course.

## ACKNOWLEDGMENTS

BR was supported by the IITB-Monash Academy. We thank Michael Coffey for making figure 31.

- <sup>1</sup>H. Aref, J. R. Blake, M. Budišić, J. H. E. Cartwright, H. J. H. Clercx, U. Feudel, R. Golestanian, E. Guillard, Y. L. Guer, G. F. van Heijst, T. S. Krasnopolskaya, R. S. MacKay, V. V. Meleshko, G. Metcalfe, I. Mezić, A. P. S. de Moura, K. E. Omari, O. Piro, M. F. M. Speetjens, R. Sturman, J.-L. Thiffeault, and I. Tuval, *Reviews of Modern Physics* **89**, 025007 (66 pages) (2017).
- <sup>2</sup>I. Mezić and S. Wiggins, *Nonlinear Science* **4**, 157 (1994).
- <sup>3</sup>G. Haller and I. Mezić, *Nonlinearity* **11**, 319 (1998).
- <sup>4</sup>S. Wiggins, *Journal of Fluid Mechanics* **654**, 1 (2010).
- <sup>5</sup>K. Bajer, *Chaos, Solitons and Fractals* **4**, 895 (1994).
- <sup>6</sup>A. Gómez and J. D. Meiss, *Chaos* **12**, 289 (2002).
- <sup>7</sup>P. Shankar and M. Deshpande, *Annual Review of Fluid Mechanics* **32**, 93 (2000).
- <sup>8</sup>C. Truesdell and W. Noll, *The Non-Linear Field Theories of Mechanics*, 3rd ed. (Springer, 2004).
- <sup>9</sup>D. Lester, M. Rudman, G. Metcalfe, and H. Blackburn, *Journal of Computational Physics* **227**, 3032 (2008).
- <sup>10</sup>M. Speetjens, E. Demissie, G. Metcalfe, and H. Clercx, *Physics of Fluids* **26**, 113601 (2014).

- <sup>11</sup>K. Petkovic, G. Metcalfe, H. Chen, Y. Gao, M. Best, D. Lester, and Y. Zhu, *Lab on a Chip* **17**, 169 (2017).
- <sup>12</sup>M. Trefry, D. Lester, G. Metcalfe, A. Ord, and K. Regenauer-Lieb, *Journal of Contaminant Hydrology* **127**, 15 (2012).
- <sup>13</sup>M. S. Cho, F. Solano, N. R. Thomson, M. G. Trefry, D. R. Lester, and G. Metcalfe, *Groundwater Monitoring & Remediation* **39**, 23 (2019), <https://ngwa.onlinelibrary.wiley.com/doi/pdf/10.1111/gwmr.12339>.
- <sup>14</sup>H. Blackburn and S. Sherwin, *Journal of Computational Physics* **197**, 759 (2004).
- <sup>15</sup>B. Ravu, M. Rudman, G. Metcalfe, D. R. Lester, and D. V. Khakhar, *Journal of Computational Physics* **323**, 75 (2016).
- <sup>16</sup>M. Speetjens, G. Metcalfe, and M. Rudman, *Physics of Fluids* **18**, 1 (2006).
- <sup>17</sup>G. Metcalfe, “Complex physical, biophysical, and econophysical systems,” (World Scientific, 2010) Chap. Applied Fluid Chaos: Designing Advection with Periodically Reoriented Flows for Micro to Geophysical Mixing and Transport Enhancement, pp. 189–242.
- <sup>18</sup>V. Malyuga, V. Melesko, M. Speetjens, H. Clercx, and G. van Heijst, *Proceedings of the Royal Society A* **458**, 1867 (2002).
- <sup>19</sup>M. Speetjens, H. Clercx, and G. van Heijst, *Journal of Fluid Mechanics* **514**, 77 (2004).
- <sup>20</sup>M. Speetjens, H. Clercx, and G. van Heijst, *Physics of Fluids* **18**, 083603 (2006).
- <sup>21</sup>M. Speetjens, H. Clercx, and G. van Heijst, *Chaos* **16**, 043104 (2006).
- <sup>22</sup>Z. Pouransari, M. Speetjens, and H. Clercx, *Journal of Fluid Mechanics* **654**, 5 (2010).
- <sup>23</sup>J. H. E. Cartwright, M. Feingold, and O. Piro, *Journal of Fluid Mechanics* **316**, 259 (1996).
- <sup>24</sup>N. R. Moharana, M. F. M. Speetjens, R. R. Trieling, and H. J. H. Clercx, *Physics of Fluids* **25**, 093602 (2013), doi:10.1063/1.4819901.
- <sup>25</sup>L. D. Smith, M. Rudman, D. R. Lester, and G. Metcalfe, *Chaos* **26**, 053106 (2016).
- <sup>26</sup>Y. A. Kuznetsov, *Elements of Applied Bifurcation Theory*, 2nd ed., Applied Mathematical Sciences (Springer-Verlag, 1998).
- <sup>27</sup>H. R. Dullin, J. D. Meiss, and D. Sterling, *Nonlinearity* **13**, 203 (1999).
- <sup>28</sup>P. Mullowney, K. Julien, and J. Meiss, *SIAM Journal on Applied Dynamical Systems* **4**, 159 (2005), <https://doi.org/10.1137/040606727>.
- <sup>29</sup>H. E. Lomelí and J. D. Meiss, *Nonlinearity* **11**, 557 (1998).
- <sup>30</sup>M. S. Chong, A. E. Perry, and B. J. Cantwell, *Physics of Fluids A* **2**, 765 (1990).
- <sup>31</sup>V. Gelfreich, *Proceedings of the National Academy of Sciences* **99**, 13975 (2002).
- <sup>32</sup>R. G. Littlejohn, *Journal of Mathematical Physics* **20**, 2445 (1979).

## Appendix A: Computational Details

### 1. Velocity Discontinuity

There is a velocity discontinuity at the rim of the hemisphere where the sliding lid meets the stationary hemisphere wall. Due to the spectral nature of *semtex*, discontinuities present significant difficulty. To handle this we replace the discontinuity in velocity with a continuous function that rapidly ramps the lid velocity from zero to 1 over a small region at the rim. The lid velocity function we use is  $U_w = 1 - e^{-2000(1-x^2)^3}$ , which is plotted in figure 27.

In order to remove the singular coordinate from the

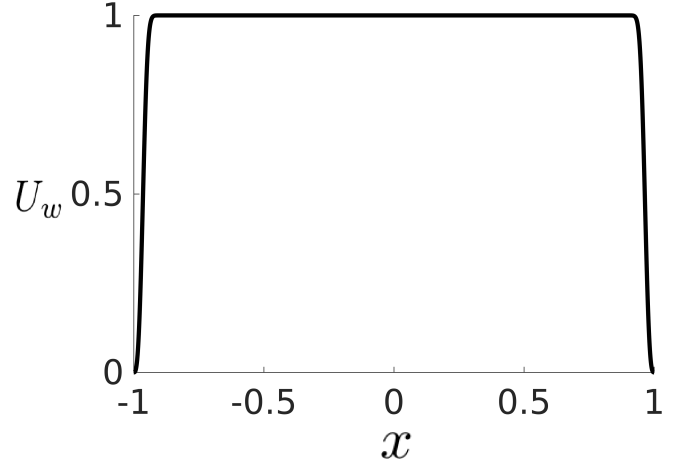


FIG. 27: Lid Velocity  $U_w$  along the  $x$  axis used in numerical computation to smooth the discontinuous boundary condition along the rim.

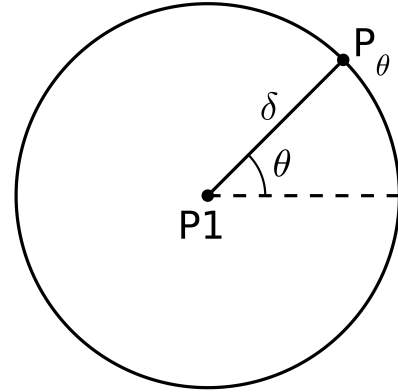


FIG. 28: Bootstrap method to approximate a periodic line. At a known point P1 on the line the circle, centred on P1 and drawn in the symmetry plane  $S_\theta$  locates the next point at  $P_\theta$ .

interior of the domain that arises when  $\sin \theta = 0$ , we preferred to use a hemispherical domain specified by  $r \in [0, 1]$ ,  $\theta \in [0, \pi]$ , and  $\phi \in [0, \pi]$ , where  $\theta$  is the polar angle and  $\phi$  is the azimuthal angle (instead of  $\theta \in [0, \pi/2]$  and  $\phi \in [-\pi, \pi]$ ). The computational method of Ravu *et al.*<sup>15</sup> fits a 3D spline to the velocity field obtained from *semtex* in a manner that ensures the resulting analytic velocity field is exactly divergence-free everywhere. We found that identification of periodic lines and Lagrangian structures was critically dependent on this divergence-free interpolation; other (high-order) interpolation schemes were unable to provide the level of accuracy required to properly resolve the coherent Lagrangian structures from a purely numerical data set.

## 2. Period-1 Lines and their Stability

In order to determine the P1 line, we start at the central fixed point,  $(r_s, \pi/2, \pi/2)$ . We know from symmetry that this point is on a line that goes from the origin  $(0, \pi/2, \pi/2)$  to the base of the hemisphere  $(1, \pi/2, \pi/2)$ . On this line,  $V_\phi$  changes sign and has a value of zero at the central fixed point. We use bisection to find  $r_s \approx 0.2589$ . P1 consists of two curve segments: the upper part  $P1_U$  from the central fixed point to the attachment point on the lid and the lower part  $P1_L$  from the central fixed point to the attachment point at the apex of the hemisphere. We compute  $P1_U$  and  $P1_L$  separately with the following algorithm.

We choose a small increment,  $\delta$ , and create a circle of this radius centred around a known P1 point on the symmetry plane (initially the central fixed point). P1 intersects this circle at two points, and we choose one,  $P_\theta$  (figure 28). As  $\{\Phi_{\beta/2}(\mathbf{x}_{P1})\}_x = 0$  for a period-1 point  $\mathbf{x}_{P1}$  (figure 29a and figure 29b), the  $x$ -component (i.e.  $\{\Phi_{\beta/2}(P_\theta)\}_x$ ) changes sign around the circle and is zero where P1 intersects the circle. Again, we use bisection to find the value of  $\theta$  at which P1 intersects the circle. The value of  $P_\theta$  becomes the starting point for the next iteration of the algorithm.

We determine the stability of P1 by expanding  $\Psi_T(\mathbf{x})$  at a period-1 point  $\mathbf{x}_{P1}$  as

$$\Psi_T(\mathbf{x}_{P1} + d\mathbf{x}) = \mathbf{x}_{P1} + \left. \frac{\partial \Psi_T}{\partial \mathbf{x}} \right|_{\mathbf{x}=\mathbf{x}_{P1}} d\mathbf{x} + \mathcal{O}(d\mathbf{x}^2), \quad (\text{A1})$$

where  $\mathbf{F} = \frac{\partial \Psi_T}{\partial \mathbf{x}}$  is the deformation tensor that we compute numerically using central differences. The two eigenvalues of  $\mathbf{F}$  not equal to one determine the stability of the period-1 point. If they are real, the point is hyperbolic; if they are complex, the point is elliptic.

## 3. Calculation of higher order periodic lines of PRHF in the Stokes regime

We show in this section how to calculate the period- $n$  lines which go through an  $n^{\text{th}}$  order degenerate point on the P1 line. To compute a period- $n$  line requires an initial period- $n$  point, which can be any point on that line. So, a period- $n$  line is computed here in two steps: 1) calculate any one period- $n$  point on the period- $n$  line, 2) calculate the full period- $n$  line using the initial period- $n$  point. In section III, the central role that degenerate points play in higher order periodicities are discussed. Without going into detail here, these will provide a starting guess for higher order points. For example,  $n$  period- $n$  lines intersect at an  $n^{\text{th}}$  order degenerate point on a P1 line. This  $n^{\text{th}}$  order degenerate point cannot be used as an initial period- $n$  point for all the  $n$  period- $n$  lines to calculate them because this point belongs to all the lines. To calculate these  $n$  period- $n$  lines, a separate initial period- $n$  point for every period- $n$  line is needed (i.e. total  $n$  initial

period- $n$  points). The  $n^{\text{th}}$  order degenerate point is used to calculate  $n$  initial period- $n$  points which are needed for the calculation of  $n$  period- $n$  lines. The initial  $n$  period- $n$  points are calculated first as described in section A 3 a, then the corresponding  $n$  period- $n$  lines are calculated as described in section A 3 b.

### a. Finding $n$ initial period- $n$ points

- Identify an  $n^{\text{th}}$  order degenerate point on the P1 line as described in section III A.
- Create a spherical grid of points which are almost equidistant from each other in a small sphere of radius 0.1 centred around the degenerate point. Because  $n$  period- $n$  lines intersect at this degenerate point, this sphere contains segments of all the  $n$  period- $n$  lines.
- Calculate the magnitude of the displacement function  $\mathbf{G}^n(\mathbf{x})$  at each grid point via

$$\mathbf{G}^n(\mathbf{x}) = \Psi^n(\mathbf{x}) - \mathbf{x}. \quad (\text{A2})$$

- Arrange the grid points as an array in ascending order of  $\|\mathbf{G}^n(\mathbf{x})\|$ , since smaller values of  $\|\mathbf{G}^n(\mathbf{x})\|$  are closer to period- $n$  lines, such points are good initial guesses for Broyden's method which is used to find  $n$  initial period- $n$  points.
- The grid points which were sorted according to the magnitude of  $\mathbf{G}^n(\mathbf{x})$  are then used one by one as initial guess for Broyden's method and initial period- $n$  points are calculated.
- Continue finding period- $n$  points from the grid points until at least one separate initial period- $n$  point for every period- $n$  line is found.
- From the computed period- $n$  points, select one period- $n$  point for each period- $n$  line and use them as initial points to calculate  $n$  period- $n$  lines as described in the next section A 3 b.

### b. Calculation of a period- $n$ line using a known initial periodic point on that line

Assume  $Pn$  is a period- $n$  line to be computed, and  $\mathbf{x}_k$  is a known initial period- $n$  point on that line.  $Pn$  is divided at the point  $\mathbf{x}_k$  into two parts:  $Pn_L$  and  $Pn_R$ . These two parts are calculated separately in the same way as described below.

1. Compute the deformation tensor  $\left. \frac{\partial \Psi^n}{\partial \mathbf{x}} \right|_{\mathbf{x}=\mathbf{x}_k}$  at  $\mathbf{x}_k$ . Because the point  $\mathbf{x}_k$  belongs to the period- $n$  line, one of its eigenvalues of the deformation tensor (i.e.

$\frac{\partial \Psi^n}{\partial \mathbf{x}}|_{\mathbf{x}=\mathbf{x}_k}$ ) will be one (say  $\lambda_3 = 1$ ), and the eigenvector  $\mathbf{e}_3$  corresponding to this eigenvalue is tangent to the period- $n$  line.

2. Compute eigenvector  $\mathbf{e}_3$ .
3. Choose  $\mathbf{x}'_{k+1} = \mathbf{x}_k \pm \epsilon \mathbf{e}_3$  where the sign is chosen to ensure  $\mathbf{x}'_{k+1}$  continues segment  $\mathbf{x}_{k-1} \rightarrow \mathbf{x}_k$ .  $\epsilon = 5 \times 10^{-3}$  is used. Note: In the first iteration, to calculate  $\mathbf{x}'_{k+1}$ , a minus sign is used in the calculation of  $Pn_L$  and a plus sign is used in the calculation of  $Pn_R$ . The signs can be interchanged in the first iteration, but the important thing is different signs must be used in the calculation of  $Pn_L$  and  $Pn_R$ . This makes the search for periodic points of  $Pn_L$  and  $Pn_R$  line segments happen in opposite directions from the initial periodic point.
4. Create a sphere centred at  $\mathbf{x}'_{k+1}$  with radius  $\epsilon/5$  and search for the root of equation A2 inside the sphere using Broyden's method to find  $\mathbf{x}_{k+1}$  which is the next period- $n$  point on the line after  $\mathbf{x}_k$ . If the root is not found within the desired convergence value ( $10^{-9}$ ), increase the radius of the sphere and do the same process again to find  $\mathbf{x}_{k+1}$ ; this process, which will always find the root, is continued until the root is found within the desired convergence value.
5. Continue steps (1) to (4) recursively to calculate period- $n$  points along the line until the line touches the boundary or the line reaches the initial point if the periodic line is closed, because a periodic line can be closed or its ends are attached to the boundary (see Appendix B).

## Appendix B: Non-existence of isolated periodic points

In principle, in a one-invariant flow a coordinate transformation can be used to map fluid particle positions  $(x, y, z)$  to  $\boldsymbol{\xi}(\theta_1, \theta_2, I)$ , where  $I$  is the action variable and  $(\theta_1, \theta_2)$  are angle variables.

$$\boldsymbol{\xi} = \begin{bmatrix} \theta_1 \\ \theta_2 \\ I \end{bmatrix} \quad (\text{B1})$$

When the system parameters  $\Theta$  and  $\beta$  are fixed, a map can be defined as

$$\boldsymbol{\xi} \mapsto \mathbf{f}(\boldsymbol{\xi}), \quad (\text{B2})$$

where  $\mathbf{f}$  is continuous in  $(\theta_1, \theta_2, I)$ .  $\boldsymbol{\xi}_0, \boldsymbol{\xi}_1, \boldsymbol{\xi}_2, \dots, \boldsymbol{\xi}_k$  is a fluid particle orbit for  $k$  periods, where

$$\boldsymbol{\xi}_n = \mathbf{f}(\boldsymbol{\xi}_{n-1}), \quad n = 1, 2, 3, \dots, k. \quad (\text{B3})$$

The period- $n$  fixed point equation, by definition, is

$$\mathbf{f}^n(\boldsymbol{\xi}) - \boldsymbol{\xi} = 0. \quad (\text{B4})$$

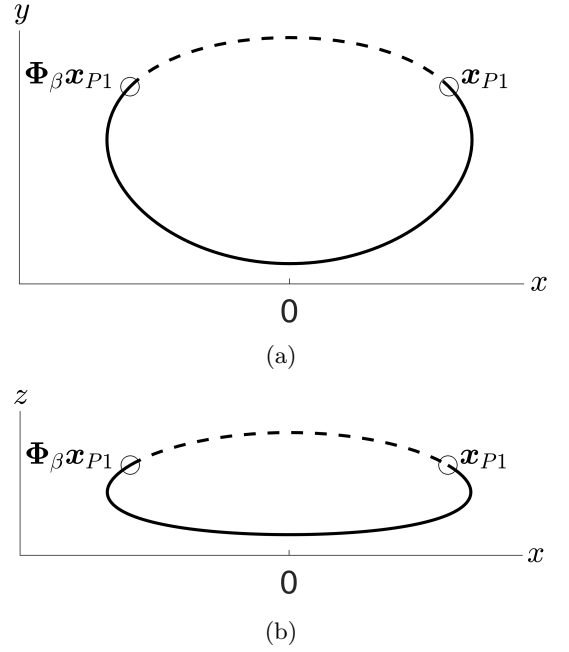


FIG. 29: Projection of a stream line of the base flow: (a)  $x$ - $y$  projection and (b)  $x$ - $z$  projection.

Since  $\mathbf{f}$  and  $\boldsymbol{\xi}$  are three-dimensional vectors, equation B4 can be split component wise into three equations as

$$f_1^n(\theta_1, \theta_2, I) - \theta_1 = 0, \quad (\text{B5a})$$

$$f_2^n(\theta_1, \theta_2, I) - \theta_2 = 0, \quad (\text{B5b})$$

$$f_3^n(\theta_1, \theta_2, I) - I = 0 \Rightarrow I - I = 0. \quad (\text{B5c})$$

Because the action variable of a fluid particle does not change in the Stokes flow, equation B5c is not an independent equation (i.e. this equation is satisfied at every point in the domain). Equations B5a and B5b represent two-dimensional surfaces that are either closed or attached to the boundary, and the intersection of these two surfaces is the solution of equation B5 which is the same as equation B4. If the two surfaces intersect (i.e. if the solution exists for some order of period  $n$ ), the intersection must be a line and cannot be a point. So equation B4 cannot have point solutions. Hence, isolated period-1 points cannot exist in the PRHF in the Stokes limit. Periodic lines with their ends attached to the boundary or closed periodic lines are possible.

## Appendix C: P1 Points Lie in the Symmetry Plane

Consider a P1 point  $\mathbf{x}_{P1}$ . We prove that this point must lie on the symmetry plane  $\mathbf{I}_\Theta$  by the following steps.

From the definition of a period-1 point

$$\mathbf{x}_{P1} = \Psi_T \mathbf{x}_{P1} = R_{-\Theta} \Phi_\beta \mathbf{x}_{P1}. \quad (\text{C1})$$

Applying  $R_\Theta$  to both sides of equation C1, we find that

$$R_\Theta \mathbf{x}_{P1} = \Phi_\beta \mathbf{x}_{P1}. \quad (\text{C2})$$

Now consider separately how each coordinate of  $\mathbf{x}_{P1}$  is modified by application of the map  $\Phi_\beta$ . Because the point  $\Phi_\beta \mathbf{x}_{P1}$  must be rotated to complete one full period of the reoriented flow map (equation C1) then  $\Phi_\beta \mathbf{x}_{P1} \neq \mathbf{x}_{P1}$ . Because rotation about the  $y$ -axis does not change the  $y$ -coordinate of a point, application of  $R_\Theta$  to  $\mathbf{x}_{P1}$  results in

$$(R_\Theta \mathbf{x}_{P1})_y = (\mathbf{x}_{P1})_y, \quad (\text{C3})$$

or from equation C2

$$(\Phi_\beta \mathbf{x}_{P1})_y = (\mathbf{x}_{P1})_y, \quad (\text{C4})$$

i.e. the  $y$ -coordinate of a period-1 point is not changed by application of the base flow (figure 29a). Because streamlines of the base flow are symmetric about  $x = 0$  and the  $y$  components of  $\mathbf{x}_{P1}$  and  $\Phi_\beta \mathbf{x}_{P1}$  are the same, we see from figures 29a and 29b that it must also be true that

$$\begin{aligned} (\Phi_\beta \mathbf{x}_{P1})_z &= (\mathbf{x}_{P1})_z \\ (\Phi_\beta \mathbf{x}_{P1})_x &= -(\mathbf{x}_{P1})_x. \end{aligned} \quad (\text{C5})$$

Equations C4 and C5 can then be written without reference to coordinate directions as

$$\Phi_\beta \mathbf{x}_{P1} = S_x \mathbf{x}_{P1}. \quad (\text{C6})$$

By substituting equation C6 into equation C2, we get

$$\begin{aligned} R_\Theta \mathbf{x}_{P1} &= S_x \mathbf{x}_{P1} \\ \mathbf{x}_{P1} &= R_{-\Theta} S_x \mathbf{x}_{P1}, \end{aligned} \quad (\text{C7})$$

and by replacing  $R_{-\Theta} S_x$  by  $S_\Theta$  (equation 14) obtain

$$\mathbf{x}_{P1} = S_\Theta \mathbf{x}_{P1}. \quad (\text{C8})$$

Hence  $\mathbf{x}_{P1} \in \mathbf{I}_\Theta$ , i.e.  $P1$  points must lie on the symmetry plane  $\mathbf{I}_\Theta$ .

#### Appendix D: Invariants of deformation tensor

As well as of using eigenvalues of deformation tensor  $\mathbf{F}$  to determine stability, invariants of  $\mathbf{F}$  (the trace  $\tau$ , the second trace  $\sigma$  and the determinant  $\det(\mathbf{F})$ ), which are discussed in section III A) can also be used. The characteristic equation for eigenvalues  $\lambda$  of a deformation tensor  $\mathbf{F}$  is given by

$$p(\lambda) = \lambda^3 - (\text{Tr } \mathbf{F})\lambda^2 + \frac{1}{2}((\text{Tr } \mathbf{F})^2 - \text{Tr } \mathbf{F}^2)\lambda - \det(\mathbf{F}), \quad (\text{D1})$$

where

$$\text{Tr } \mathbf{F} = \tau = \lambda_1 + \lambda_2 + \lambda_3 \quad (\text{D2})$$

and the term  $\frac{1}{2}((\text{Tr } \mathbf{F})^2 - \text{Tr } \mathbf{F}^2)$  in equation D1 is the second trace  $\sigma$ .

$$\sigma = \frac{1}{2}((\text{Tr } \mathbf{F})^2 - \text{Tr } \mathbf{F}^2) = \lambda_1 \lambda_2 + \lambda_2 \lambda_3 + \lambda_3 \lambda_1 \quad (\text{D3})$$

Because  $\det(\mathbf{F}) = 1$  for volume preserving maps, the characteristic equation of the Deformation Tensor  $\mathbf{F}$  can be written as,

$$p(\lambda) = \lambda^3 - \tau\lambda^2 + \sigma\lambda - 1. \quad (\text{D4})$$

Because  $\lambda_3 = 1$  (by definition from section III A) and  $\det(\mathbf{F}) = 1$ , we can write,

$$\lambda_2 = 1/\lambda_1. \quad (\text{D5})$$

Substituting equation D5 in equation D3, we get

$$\begin{aligned} \sigma &= \lambda_1 \lambda_2 + \lambda_2 \lambda_3 + \lambda_3 \lambda_1 \\ &= 1 + 1/\lambda_1 + \lambda_1 \\ &= \tau. \end{aligned} \quad (\text{D6})$$

Since  $\tau = \sigma$  and  $\det(\mathbf{F}) = 1$ , the stability of a period-1 point depends only on one invariant, which is  $\tau$  of the deformation tensor.

The characteristic equation D4 can be written as,

$$\begin{aligned} p(\lambda) &= \lambda^3 - \tau(\lambda^2 - \lambda) - 1 \\ &= (\lambda - 1)(\lambda^2 + (1 - \tau)\lambda + 1). \end{aligned} \quad (\text{D7})$$

The solutions of this equation are 1 and  $\frac{1}{2}((\tau - 1) \pm \sqrt{\tau^2 - 2\tau - 3})$ . We can characterize the nature of a period-1 point of a period-1 line line by calculating the trace of the deformation tensor evaluated at that point. If  $\tau \in (-1, 3)$ , the term  $\tau^2 - 2\tau - 3$  is negative, the period-1 point is elliptic. If  $\tau > 3$ , then the period-1 point is hyperbolic, if  $\tau < -1$ , then the period-1 point is hyperbolic.

#### Appendix E: Surviving Invariant and Hamiltonian Flow

Here we show that the rotation of the base flow leaves one invariant and that the motion on each spheroidal shell is Hamiltonian. The proof is more general than the hemisphere, being true for any container generated by any figure of revolution of a convex line terminating on a plane that is the moving lid of the container.

Although the following proof uses a different coordinate system for the hemisphere to that shown in figure 1, this difference is purely cosmetic. Note 1: Here we treat  $\theta$  as the azimuthal angle and  $\phi$  as the polar angle. In the rest of the paper we treated  $\theta$  as the polar angle and  $\phi$  as the azimuthal angle. Note 2: In our computations of PRHF, the lid coincides with the  $x$ - $z$  plane and translates in the  $\hat{\mathbf{x}}$  direction. Only in this appendix does the lid coincide with the  $x$ - $y$  plane and translate in the  $\hat{\mathbf{x}}$ .

Consider Stokes flow inside a container driven by a solid boundary coincident with the  $x$ - $y$  plane and uniformly translating in the  $\hat{\mathbf{x}}$  direction at a steady speed  $U_w$ . The equations of motion for the fluid inside the domain are given by equations 2 and 3. Any container having the  $x$ - $y$  plane as the sliding lid and obtained via a

surface of revolution about the  $z$ -axis of a curve in the  $x$ - $y$  plane is left-right ( $z$ -direction) and fore-aft ( $x$ -direction) symmetric. If the curve is convex, so that the container is left-right and fore-aft symmetric, then the velocity field components  $\mathbf{U} = (U_r, U_\phi, U_\theta)$  have the form

$$U_r = u_r(r, \phi) \cos \theta, \quad (\text{E1a})$$

$$U_\phi = u_\phi(r, \phi) \cos \theta, \quad (\text{E1b})$$

$$U_\theta = u_\theta(r, \phi) \sin \theta \quad (\text{E1c})$$

in spherical coordinates. The most general container to which this analysis applies starts with a curve in the  $x$ - $z$  plane connecting the  $z$  axis to the  $x$  axis. This curve then generates a surface of revolution about the  $z$ -axis that is the container shape with the  $x$ - $y$  plane the sliding lid of the container. The doubly symmetric container and symmetric driving plane, assumed without loss of generality to move in the  $x$  direction, produce a Stokes flow with a reflection symmetry across the  $x$ -axis and a time-reversal symmetry across the  $y$ -axis.

Having two symmetries, the flow has two invariants of the motion  $F_{1,2}$ , both given by

$$\mathbf{U} \cdot \nabla F_{1,2} = 0; \quad (\text{E2})$$

moreover, equations E1 imply that the invariant surfaces have the form

$$F_{1,2}(r, \phi, \theta) = f_{1,2}(r, \phi)g(\theta). \quad (\text{E3})$$

Following Malyuga et al.<sup>18</sup>, putting equations E3 and E1 into equation E2 gives

$$u_r \cos \theta \frac{\partial f}{\partial r} + \frac{u_\phi \cos \theta}{r} g \frac{\partial f}{\partial \phi} + \frac{u_\theta \sin \theta}{r \sin \phi} f \frac{\partial g}{\partial \theta} = 0, \quad (\text{E4})$$

where  $f$  is either of the 2-dimensional invariants. Equation E4 is separable, and the equation for  $g$  is

$$\sin \theta \frac{dg}{d\theta} - \lambda g \cos \theta = 0, \quad (\text{E5})$$

where  $\lambda$  is the separation constant. For  $\lambda = 0$   $g$  is a constant that, without loss of generality, can be set to one. For  $\lambda = 1$ ,  $g = \sin \theta$ . Therefore the two invariants are

$$F_1 = f_1(r, \phi), \quad (\text{E6})$$

$$F_2 = f_2(r, \phi) \sin \theta. \quad (\text{E7})$$

The equation for  $f$  is

$$u_r \frac{\partial f}{\partial r} + \frac{u_\phi}{r} \frac{\partial f}{\partial \phi} + \frac{\lambda u_\theta}{r \sin \phi} f = 0. \quad (\text{E8})$$

From equation E2, the two invariant surfaces intersect at stream lines of the flow, and the equations for the two invariant surfaces are

$$\lambda = 0 \quad \mathbf{u}' \cdot \nabla' f_1 = 0, \quad (\text{E9})$$

$$\lambda = 1 \quad \mathbf{u}' \cdot \nabla' f_2 = -\frac{u_\theta}{r \sin \phi} f_2, \quad (\text{E10})$$

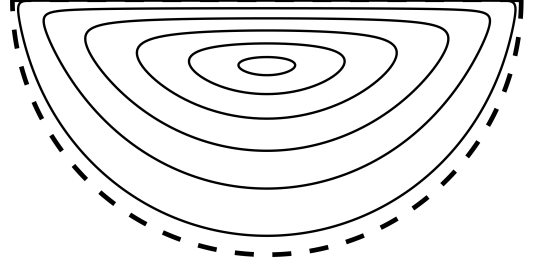


FIG. 30: Flow cross-section of streamlines in the  $x$ - $y$  plane. Dashed line is the hemisphere and lid boundary. The lid moves left to right in the  $+x$  direction.

where  $\mathbf{u}' = (u_r, u_\phi)$  and  $\nabla' = (\partial/\partial r, r^{-1}\partial/\partial\phi)$ .

From  $\nabla \cdot \mathbf{U} = 0$  the azimuthal velocity required to satisfy continuity is

$$\left(\frac{2}{r} + \frac{\partial}{\partial r}\right) u_r + \left(\frac{1}{r} + \frac{\partial}{\partial \phi} + \frac{\cot \phi}{r}\right) u_\phi = \frac{-u_\theta}{r \sin \phi}. \quad (\text{E11})$$

Combining equations E11 and E9 shows that

$$\frac{1}{r} \frac{\partial f_1}{\partial \phi} = \frac{u_r r^2 \sin \phi}{f_2} \quad (\text{E12a})$$

$$-\frac{\partial f_1}{\partial r} = \frac{u_\phi r^2 \sin \phi}{f_2} \quad (\text{E12b})$$

$$\nabla \cdot \left( \frac{\mathbf{u}' r^2 \sin \phi}{f_2} \right) = 0, \quad (\text{E12c})$$

or more compactly by defining  $\mathbf{u}^* \equiv \mathbf{u}' r^2 \sin \phi / f_2$  that

$$\frac{1}{r} \frac{\partial f_1}{\partial \phi} = u_r^*(r, \phi) \quad (\text{E13a})$$

$$-\frac{\partial f_1}{\partial r} = u_\phi^*(r, \phi) \quad (\text{E13b})$$

$$\nabla \cdot \mathbf{u}^* = 0. \quad (\text{E13c})$$

The Hamiltonian form of equations E13 reveals the invariant  $f_1$  as a streamfunction in the  $r - \phi$  plane for the rescaled solenoidal vector field  $\mathbf{u}^*$ . A cross-section of  $f_1$  is shown in figure 30. For periodic reorientation  $F_2$  is destroyed, but  $F_1$ , being rotationally symmetric, is preserved. In other words, the Hamiltonian structure is locally preserved. In the action-angle formalism,  $F_1$  is the conserved action, and the periodically reoriented lid-driven cavity flow in a doubly-symmetric container is an action-angle dynamical system.

The form of equations E12, which are essentially the same as found for a cylindrical container by Malyuga et al.<sup>18</sup>, suggests a more general perspective is possible, which is that all periodically reoriented Stokes flows in

containers of revolution with a moving lid can be put into a Darboux standard form. Notice that equations E12 can be put into the noncanonical Hamiltonian-Poisson form

$$\frac{d\mathbf{x}}{dt} = \frac{f_2}{J} F_c \cdot \nabla H, \quad (\text{E14})$$

with  $\mathbf{x} = (r, \phi)^T$ ,  $H = f_1$  the Hamiltonian,  $J$  the Jacobian of the coordinate system, and

$$F_C = \begin{pmatrix} 0 & 1 \\ -1 & 0 \end{pmatrix} \quad (\text{E15})$$

is the canonical skew-symmetric matrix. A Poisson manifold, which we specify here for 3D only, is a mixture of canonical and noncanonical coordinates  $(q, p, z)$  with  $z$  a Casimir invariant that commutes with the Hamiltonian:  $\{z, H\} = 0$ , with  $\{\cdot, \cdot\}$  the Poisson bracket.  $(f_2/J)$ , then, is the inverse Jacobian for the squashed hemisphere coordinate system. It is easier to see the structure if we “blow up” the hemisphere into a topologically equivalent actual sphere. Then in equation E14  $f_2 \rightarrow 1$  and  $F_c$  becomes through the Darboux theorem<sup>32</sup> the 3D singular Poisson operator

$$\mathcal{J} = \begin{pmatrix} 0 & 1 & 0 \\ -1 & 0 & 0 \\ 0 & 0 & 0 \end{pmatrix}. \quad (\text{E16})$$

Now with  $\mathbf{x} = (\theta, \phi, r)^T$  equation E14 becomes

$$\frac{d\mathbf{x}}{d\tau} = \mathcal{J} \cdot \nabla H, \quad (\text{E17})$$

where the Jacobian has been absorbed into a reparameterization of time. The dynamical system E17 is Hamiltonian on level sets of the Casimir function  $r = \text{constant}$ . The Casimir invariant—here the radial coordinate after conformal transformation to a sphere—is a topological constraint to a foliation of Hamiltonian leaves. In the squashed hemisphere coordinates, what we have called the action coordinate or shell number is the Casimir function and  $\mathcal{J}$  is a skew-symmetric matrix of generalized structure functions associated with the conformal transform of sphere to hemisphere. We do not calculate the structure functions, but all lid-driven cavities of Stokes flow are reducible to the Hamiltonian-Poisson form of equation E17 with appropriate structure functions.

#### Appendix F: Lid Attachment Point for $\beta \leq 1$

With reference to the inset of figure 31 the P1 attachment point on the lid is the point that begins on the symmetry plane a distance  $R_l$  from the center of the lid along the symmetry plane and is displaced an amount  $\beta$  such that subsequent rotation by  $-\Theta$  returns the point to its initial position. A trigonometric relations gives

$$R_l = \frac{\beta}{2 \sin(\frac{\Theta}{2})} \quad (\text{F1})$$

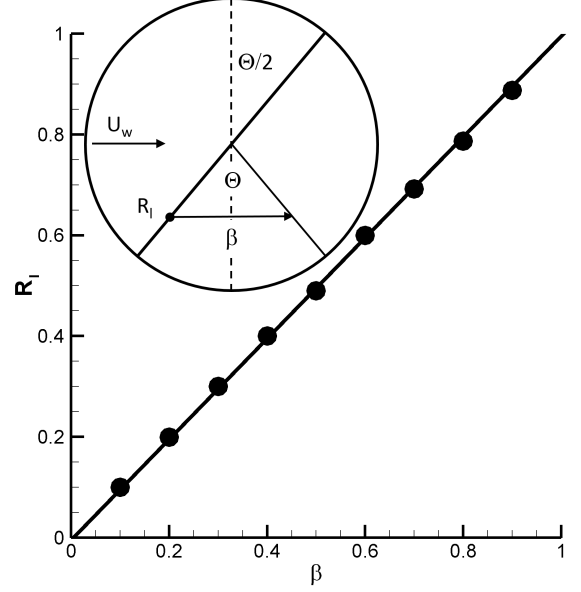


FIG. 31: The attachment point on the lid starts at the origin for  $\beta = 0$  and moves to the rim for increasing  $\beta \leq 1$ . Plotted is the lid attachment point's distance  $R_l$  from the origin to the rim as a function of  $\beta$  for  $\Theta = \pi/3$ . Dots are computations; solid line is equation F1. Inset is geometry to determine location of the P1 attachment point.

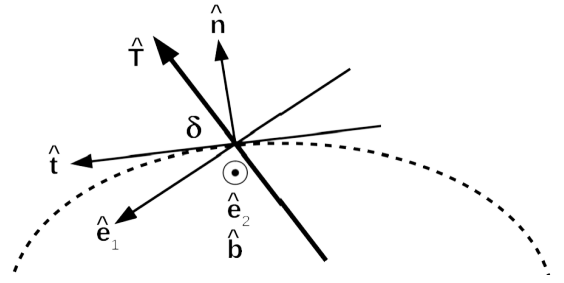


FIG. 32: Shell (dashed line) pierced by periodic line with  $\hat{T}$  the tangent null direction of the periodic line.  $\hat{e}_1$  and  $\hat{e}_2$  are the other eigendirections of the deformation tensor at the piercing point, and  $\hat{n}$ ,  $\hat{t}$ , and  $\hat{b}$  are respectively the normal, tangent, and binormal unit vectors of the shell at the piercing point.  $\hat{b}$  is normal to the page and  $\delta$  is the angle between the normal plane of the shell and the deformation plane perpendicular to  $\hat{T}$ .

for any  $\Theta$  and  $\beta \leq 1$ . Figure 31 shows equation F1 as a solid line and numerically determined locations of the attachment point as dots.

### Appendix G: Extrema of Parameterised Periodic Lines

Figure 32 depicts a generic neighbourhood around a point at which P1 pierces a shell. At the piercing point the shell is described by its normal, tangent and binormal unit vectors,  $(\hat{n}, \hat{t}, \hat{b})$ , with  $(\hat{t}, \hat{b})$  defining the tangent plane of the shell. The eigendirections of the deformation tensor at the piercing point are designated  $(\hat{T}, \hat{e}_1, \hat{e}_2)$  in the figure.  $\hat{T}$  is tangent to the line and is a null direction of deformation because the point is part of P1 and the invariance precludes normal (off-shell) transport. The other eigendirections of the deformation tensor at the piercing point,  $(\hat{e}_1, \hat{e}_2)$ , define a deformation plane perpendicular to  $\hat{T}$ . Without loss of generality we can make a local coordinate transformation at the shell and rotate the shell's tangent vector  $\hat{t}$  so that the periodic line's tangent  $\hat{T}$  is in the plane  $(\hat{n}, \hat{t})$ . This also has the effect of making  $\hat{e}_2$  and  $\hat{b}$  coincide, as in the figure. The angle  $\delta$  is the angle between the P1 line and the tangent plane at the point of piercing. As transport normal to the shell is forbidden, deformation in the tangent plane of the shell is given by the projection of the deformation described by  $(\hat{e}_1, \hat{e}_2)$  onto  $(\hat{t}, \hat{b})$ . Since  $\hat{e}_2$  and  $\hat{b}$  are already co-linear, this projection is  $\hat{e}_1 \sin \delta$ . The normal form for the deformation tensor in the neighbourhood of the piercing point becomes

$$\begin{pmatrix} 1 & 0 & 0 \\ 0 & \begin{pmatrix} \lambda_1 \sin \delta & 0 \\ 0 & \lambda_2 \end{pmatrix} \\ 0 & \end{pmatrix}. \quad (\text{G1})$$

Note that exchanging rows in the submatrix giving deformation in the tangent plane of the shell in the neighbourhood of the piercing point puts the submatrix in the form of a general linear flow<sup>17</sup>, whose eigenvalues  $\sigma$  are

$$\sigma = \pm \sqrt{\lambda_1 \lambda_2 \sin \delta}. \quad (\text{G2})$$

Because streamlines cannot cross except at points with zero velocity, planar flow topology is restricted to combinations of elliptic, shear, or hyperbolic flows. The general linear flow encompasses elliptic, hyperbolic, and shear flows in one velocity gradient matrix, identical with the submatrix, with a single parameter that ranges from  $-1$  to  $1$ : negative (positive) values of the parameter give elliptic (hyperbolic) streamlines; a zero value gives a shear flow<sup>17</sup>.

The key point about equation G2 is that when a periodic line is tangent to a shell, the tangent vectors  $\hat{T}$  and  $\hat{t}$  of the line and plane coincide. Thus  $\delta$  goes to zero, forcing the deformation eigenvalues to zero, indicating a degenerate point. On either side of degenerate (tangent) points on P1, the shell number is either lower or higher than at the tangent point, indicating these points represent local extrema on the plot of shell number versus arc length. Thus local extrema in shell number versus arc length necessarily indicate the location of a degenerate point on P1. Moreover, as can be seen from equation G2 as  $\delta$  goes from just above zero to just below, the character

of the line must change. We cannot definitely determine the direction of the change because that depends on the sign of  $\lambda_2$ , but the geometry of the periodic line at the degenerate point forces a change of character (this is clearly seen in the example shown in figure 7b). If it is elliptic (hyperbolic) on one side, it must be hyperbolic (elliptic) on the other. Note that we do not say that degenerate points at extrema are the only degenerate points that exist in the flow; the idiosyncratic dynamics of a particular flow can (and does) produce other degenerate points on periodic lines. In principle P1 could be tangent to a shell, but not be a local extrema, i.e. it could be an inflexion point on the shell number *vs* arc length plot. In such cases,  $\delta$  does not change sign, instead it goes to zero then goes positive (or negative) again. Thus inflexion in P1 means a degenerate point but no change of character either side of the degenerate point.